J Neurophysiol 111: 1132–1149, 2014.
First published December 18, 2013; doi:10.1152/jn.00785.2013.

Large-scale, high-density (up to 512 channels) recording of local circuits in behaving animals

Antal Berényi,[1,2,3] Zoltán Somogyvári,[2,4] Anett J. Nagy,[3] Lisa Roux,[1] John D. Long,[1] Shigeyoshi Fujisawa,[1,2,5] Eran Stark,[1] Anthony Leonardo,[6] Timothy D. Harris,[6] and György Buzsáki[1,2,6]

[1]*New York University Neuroscience Institute, School of Medicine, New York University, New York, New York;* [2]*Center for Molecular and Behavioral Neuroscience, Rutgers, The State University of New Jersey, Newark, New Jersey;* [3]*MTA-SZTE "Momentum" Oscillatory Neuronal Networks Research Group, Department of Physiology, University of Szeged, Szeged, Hungary;* [4]*Wigner Research Center for Physics, Department of Theory, the Hungarian Academy of Sciences, Budapest, Hungary;* [5]*Laboratory for Systems Neurophysiology, RIKEN Brain Science Institute, Wako, Saitama, Japan; and* [6]*Janelia Farm Research Campus, Howard Hughes Medical Institute, Ashburn, Virginia*

Submitted 4 November 2013; accepted in final form 10 December 2013

Berényi A, Somogyvári Z, Nagy AJ, Roux L, Long JD, Fujisawa S, Stark E, Leonardo A, Harris TD, Buzsáki G. Large-scale, high-density (up to 512 channels) recording of local circuits in behaving animals. *J Neurophysiol* 111: 1132–1149, 2014. First published December 18, 2013; doi:10.1152/jn.00785.2013.—Monitoring representative fractions of neurons from multiple brain circuits in behaving animals is necessary for understanding neuronal computation. Here, we describe a system that allows high-channel-count recordings from a small volume of neuronal tissue using a lightweight signal multiplexing headstage that permits free behavior of small rodents. The system integrates multishank, high-density recording silicon probes, ultraflexible interconnects, and a miniaturized microdrive. These improvements allowed for simultaneous recordings of local field potentials and unit activity from hundreds of sites without confining free movements of the animal. The advantages of large-scale recordings are illustrated by determining the electroanatomic boundaries of layers and regions in the hippocampus and neocortex and constructing a circuit diagram of functional connections among neurons in real anatomic space. These methods will allow the investigation of circuit operations and behavior-dependent interregional interactions for testing hypotheses of neural networks and brain function.

local field potential; unit firing; monosynaptic connections; behaving rats and mice

ALTHOUGH THE EXPLORATION OF THE wiring diagram of brain networks is moving forward at an unprecedented scale (Lichtman and Denk 2011), and steady innovations in optogenetics provide a tool set for identification and manipulation of circuit components (Boyden et al. 2005; Lein et al. 2007; Madisen et al. 2012; Prakash et al. 2012; Tye and Deisseroth 2012; Yizhar et al. 2011), complementary methods for monitoring the activity of large numbers of neurons in multiple local circuits in the behaving animal are lagging (Alivisatos et al. 2013; Buzsáki 2004; Nicolelis et al. 1997). Yet, monitoring a statistically representative fraction of neurons of the investigated circuits in behaving animals is a prerequisite for understanding neuronal computation (Alivisatos et al. 2012, 2013; Buzsáki 2004; Carandini 2012; Nicolelis et al. 1997). Currently, recordings of individual neurons and local field potentials (LFPs) in local circuits at high temporal resolution are possible with wire or nanomachined microelectrodes ("silicon probes"; Blanche et al. 2005; Buzsáki 2004; Buzsáki et al. 2012; Du et al. 2011; Logothetis 2003; Wilson and McNaughton 1993). High-density probes can record from multiple cortical and subcortical structures in the freely behaving animal at the spatial resolution of single neurons (Blanche et al. 2005; Buzsáki 2004; Csicsvari et al. 2003; Du et al. 2011; Fujisawa et al. 2008; Montgomery et al. 2008). Furthermore, silicon probe recordings can be combined with optogenetic methods for the identification of neuron types and selective manipulation of local circuits (Anikeeva et al. 2012; Boyden et al. 2005; Royer et al. 2010; Stark et al. 2012).

Whereas silicon probe technology is poised to offer ever-larger site numbers and smaller volume probes (Du et al. 2009, 2011), significant improvements and miniaturization are needed at the level of headstage interconnects, signal multiplexing, ultraflexible connection between the animal and the recording equipment, and signal processing (Du et al. 2011; Szuts et al. 2011; Vandecasteele et al. 2012). One critical aspect of miniaturization is the deployment of signal multiplexers. Previously used multiplexers have either low channel counts or limited high- or low-pass frequency characteristics for simultaneous recordings of both unit and LFP signals in the physiological range (Du et al. 2011; Harrison 2008; Olsson et al. 2005; Szuts et al. 2011; Viventi et al. 2011). Below, we present the development of a high-throughput integrated microelectronic system, including high-density, multiple-shank recordings of unit activity and LFP from multiple brain regions, using on-stage signal multiplexing methods. Applications are demonstrated in freely moving rats and mice, including extension to optogenetic manipulations.

MATERIALS AND METHODS

Animal Surgery, Recording, and Behavioral Paradigms

All experiments were approved by the Institutional Animal Care and Use Committee of New York University Medical Center and the Ethical Committee for Animal Research at the Albert Szent-Györgyi Medical and Pharmaceutical Center of the University of Szeged. The experimental protocol was in agreement with the European Communities Council Directive of November 24, 1986 (86/609/EEC) and the National Institutes of Health *Guide for the Care and Use of Laboratory Animals*. Five

Address for reprint requests and other correspondence: G. Buzsáki, NYU Neuroscience Institute, New York Univ., Langone Medical Center, East River Science Park, 450 East 29th St., 9th Fl., New York, NY 10016 (e-mail: gyorgy.buzsaki@nyumc.org).

male Long-Evans rats (400–640 g; 3–10 mo old) were implanted with high-density, 256-site silicon probes under isoflurane anesthesia as described earlier (Vandecasteele et al. 2012). The probes and the polyimide interconnect cable were manufactured by NeuroNexus (http://www.neuronexus.com). In two rats, two probes were implanted; in one rat the probes were placed in the same hemisphere, whereas in the other they were placed symmetrically in the two hemispheres (Fig. 1). During surgery, the tips of the shanks are inserted into the superficial cortical layers or ~1 mm above the intended subcortical target. After recovery, the probe is moved gradually until the target layer is reached using 70- to 150-μm rotations per day until most or all shanks record units and the probe has reached the desired target. The operated animals were housed in individual cages.

Neuronal activity in the neocortex and/or the hippocampus was recorded while the animals were running in a 240-cm long linear maze, performing a delayed alternation task in a similar-sized T-maze for water reward, or freely exploring an open-field platform. The neuronal activity during rest/sleep in the home cage preceding and following the waking sessions was also recorded. The wide-band signal was low-pass filtered and downsampled to 1,250 Hz to generate the LFP and high-pass filtered (>0.8 kHz) for spike detection. Malfunctioning recording sites (due to high impedance, cross talk, and short circuit) were removed from the analysis. Operated mice (male, 8–20 wk) were also housed individually after surgery. Details of surgery, optogenetic methods, and behavioral tests are available in Stark et al. (2012).

Histology

Following the termination of the experiments, the animals were deeply anesthetized and transcardially perfused first with 0.9% saline solution

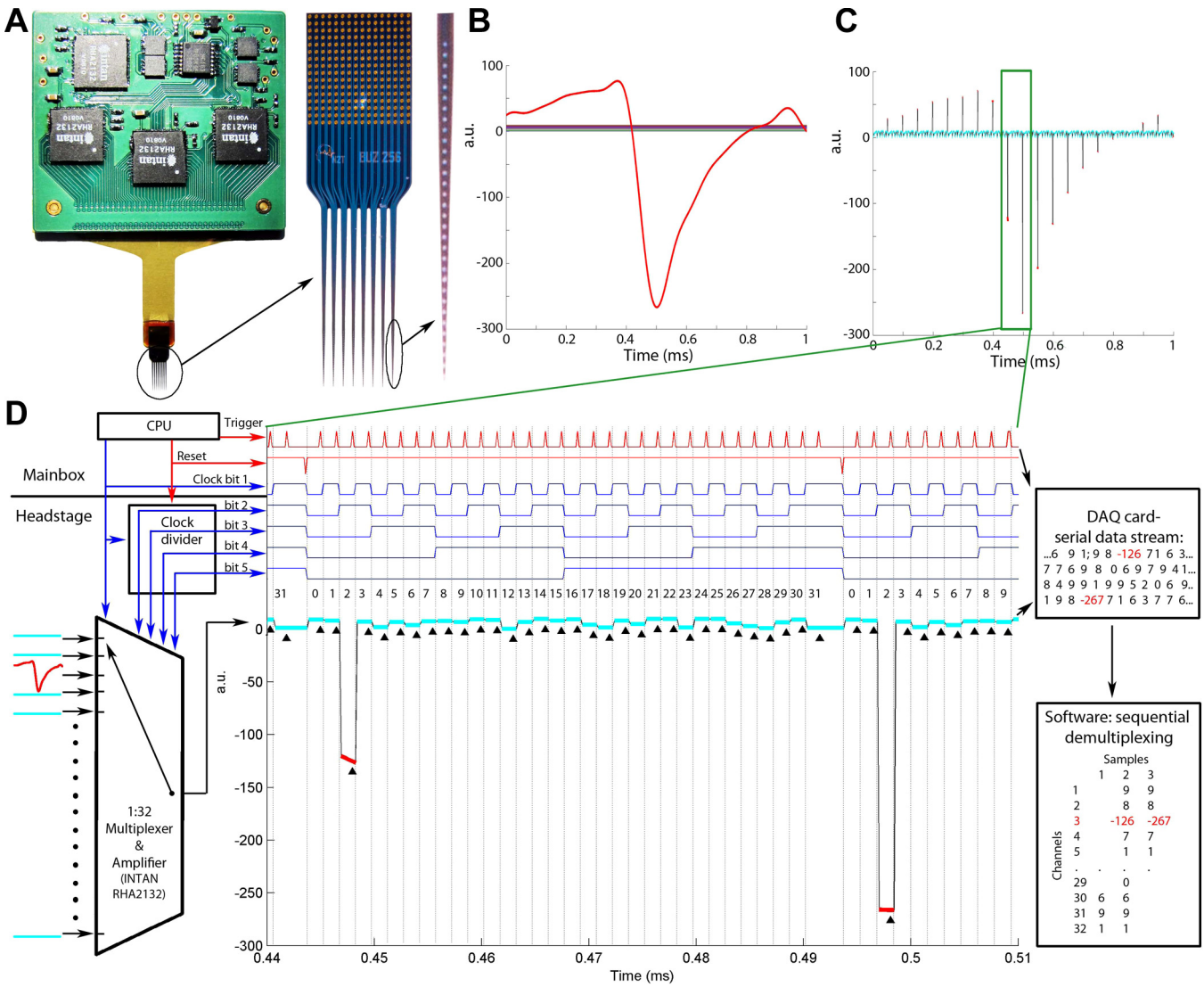

Fig. 1. System overview. *A*: high-channel-count (256 sites) silicon probe connected to a printed circuit board via a flexible polyimide ribbon cable. The printed circuit board contains 8 separate 32-channel signal multiplexers (4 on each side) and accessory circuit elements. *B*: a simulated headstage input signal illustrating a spike waveform on 1 of the 32 channels and various levels of direct current (DC) on the remaining 31 channels (1 ms). a.u., Arbitrary units. *C*: time-shared multiplexed signal transmitting the 32 channels shown in *B*. *D*: circuit schematics and working principle of the multiplexer and a zoomed segment of the time epoch shown by rectangle in *C*. The multiplexer chip receives the input signals and is driven by both the clock signal of the main microcontroller and the complementary clock bits generated by the clock divider. The horizontal line separates circuits contained in the headstage and the main box. Middle part: zoomed segment of the multiplexed signal shown in *B*. The reset line resets the clock bits to "00000" after every 32 steps to ensure the proper channel order. The trigger signal is timed to sample the "tail" of each transmitted signal snippet (marked by black triangles). The 2 large steps (red) correspond to the 2 digital samples at the trough of the spike waveform on input channel 3. Right part: numerical representation of the analog-to-digital (A/D)-converted multiplexed line (readout from the A/D card) and its demultiplexed form after the software reconstruction of the digitized samples. CPU, central processing unit.

followed by 4% formaldehyde solution. The brains were sectioned by a Vibratome (Leica) at 100 μm, parallel with the plane of the implanted silicon probes. Sections were DAPI-stained and mounted in Fluoromount (both Sigma-Aldrich). Some sections were immunostained against calbindin to determine the border between CA3 and CA2. The tracks were typically reconstructed from a few adjacent sections.

Single-Unit Analyses

Extracellular representations of action potentials were extracted from the recorded broad-band signal after high-pass filtering (>800 Hz) by a threshold crossing-based algorithm. The dimensionality of the spike waveform representations on 32 contact sites of a given shank were reduced using principal component analysis, and the individual spikes were automatically clustered into groups with the lowest possible internal variance (i.e., representing action potentials generated by single neurons) using KlustaKwik (Harris et al. 2000). The generated cluster groups were manually refined by discarding multiunit clusters showing corrupted autocorrelograms. Groups with unstable firing patterns over time were also deleted. To compare the quality of single-unit cluster isolation under various conditions, cluster qualities were estimated using the following two conjunctive measures (Harris et al. 2000; Stark et al. 2012). *1*) Cluster overlap in the high-dimensional feature space was estimated by the Mahalanobis distance (isolation distance, ID). *2*) The ratio between the frequency of spikes present within 0- to 2-ms interspike interval (ISI) and those

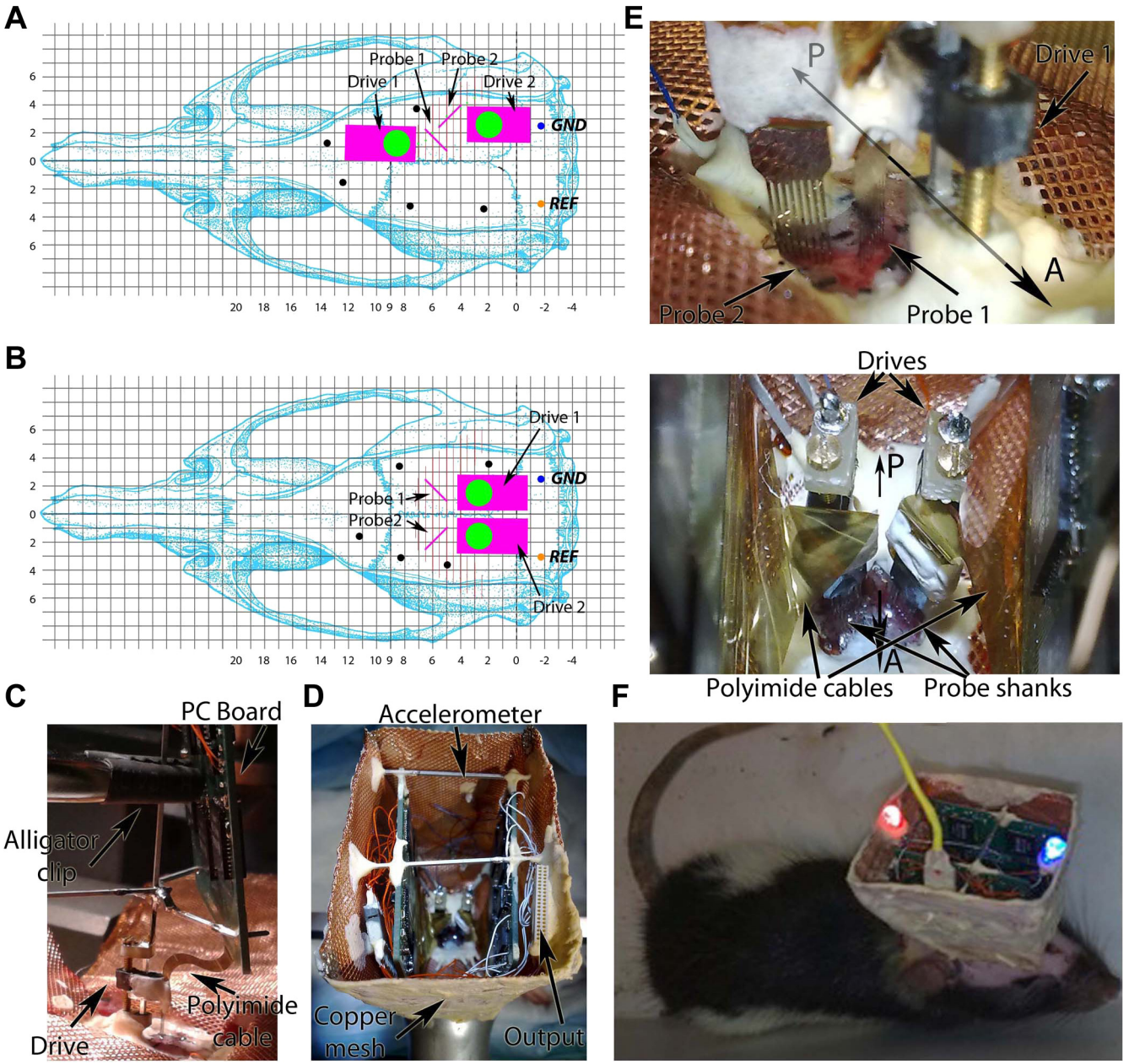

Fig. 2. Surgery details of probe implantation. *A* and *B*: skull coordinates for implantation of 2 256-site probes into the same (*A*) or 2 hemispheres (*B*). The orientation of the probe shanks is indicated by pink lines next to the probe drives. Black dots: watch screws. GND, ground; REF, reference electrode. *C*: during probe implantation, the probe and the printed circuit (PC) board are rigidly connected by brass rods, and the assembly is held by an alligator clip. The probe is fixed to the drive and connected to the PC board by a flexible polyimide cable. *D*: the headstage after implantation. The output connector, accelerometer, and copper wire mesh shield are marked by arrows. *E*: details of the probe shanks after they penetrated the brain. A, anterior; P, posterior direction. *Bottom*: top view of the implanted drives. *F*: rat equipped with 2 256-site probes during maze exploration connected to the equipment via an ultraflexible cable (yellow).

at 0- to 20-ms interval was defined as the ISI ratio and used as a measure of possible contamination of an isolated single unit by spikes of another unit. We used two levels of criteria to exclude contaminated clusters from our analyses. In the "permissive" approach clusters with either ISI ratio < 0.4 or ID > 30 were included, whereas in the "conservative" analyses clusters only with ISI ratio < 0.2 and ID > 40 were included.

The number of simultaneously recorded units (unit yield) was quantified as an average number of neurons per session per recording site overlapping with cellular layers.

For behavior-related analyses, the spatial position of the animal was sampled every 30 ms with 3-mm resolution. For LFP phase-dependent circular metrics, the phase of each LFP frequency component was determined by Hilbert-transforming the 0-phase shift, digital filtered LFP ($2 \times$ 4th-order Butterworth infinite impulse response filter).

Cross-Correlation Analysis

Monosynaptic interactions of single units were determined by the examination of the cross-correlograms. Short-latency (1–5 ms), narrow (1–2 ms) peaks or troughs (monosynaptic excitation or inhibition, respectively) were deemed significant if they crossed a global threshold band determined from a surrogate data set of 1,000 jittered spike trains (99% confidence interval, ± 0- to 4-ms jittering with uniform distribution; Fujisawa et al. 2008). For monosynaptic interaction-based network mapping (Fig. 11), the permissive data set of single units was used since a moderate contamination of the unit clusters does not introduce spurious short-latency peaks. Spike contamination increases "noise" in the cross-correlogram and, in fact, decreases the probability of finding monosynaptically connected neuron pairs.

Spike-Triggered LFP Maps

Sixty-millisecond long, low-pass filtered (<600 Hz), perispike LFP traces centered at the spike occurrences of the spike train of selected neurons were extracted. The LFP segments for each recording site were high-pass filtered (20 and 5 Hz for run and sleep sessions, respectively; 0-phase shift $2 \times$ 4th-order Butterworth infinite impulse response filter). The purpose of the higher cutoff frequency for run sessions was to eliminate the large-amplitude theta fluctuation. The filtered perispike segments were averaged across multiple spikes (usually a few thousand occurrences for run sessions and a few hundred for sharp wave-ripple segments). The mean perispike LFPs of the 256 or 512 recording channels were reordered in 2 dimensions (2-D) to match with the anatomic layout of the recording sites on the silicon probe, forming an activity map of the recorded structures. Consecutive data points in each segment were visualized as multiple frames of a movie using the following equation:

$$\mathrm{MAP}_{ij} = \frac{\tan^{-1}\left(\frac{\mathrm{LFP}_{ij}}{\mathrm{maxLFP}} \times zf\right)}{\tan^{-1}(zf)},\ i \in N\{1, \ldots, 8\},\ j \in N\{1, \ldots, 32\}$$

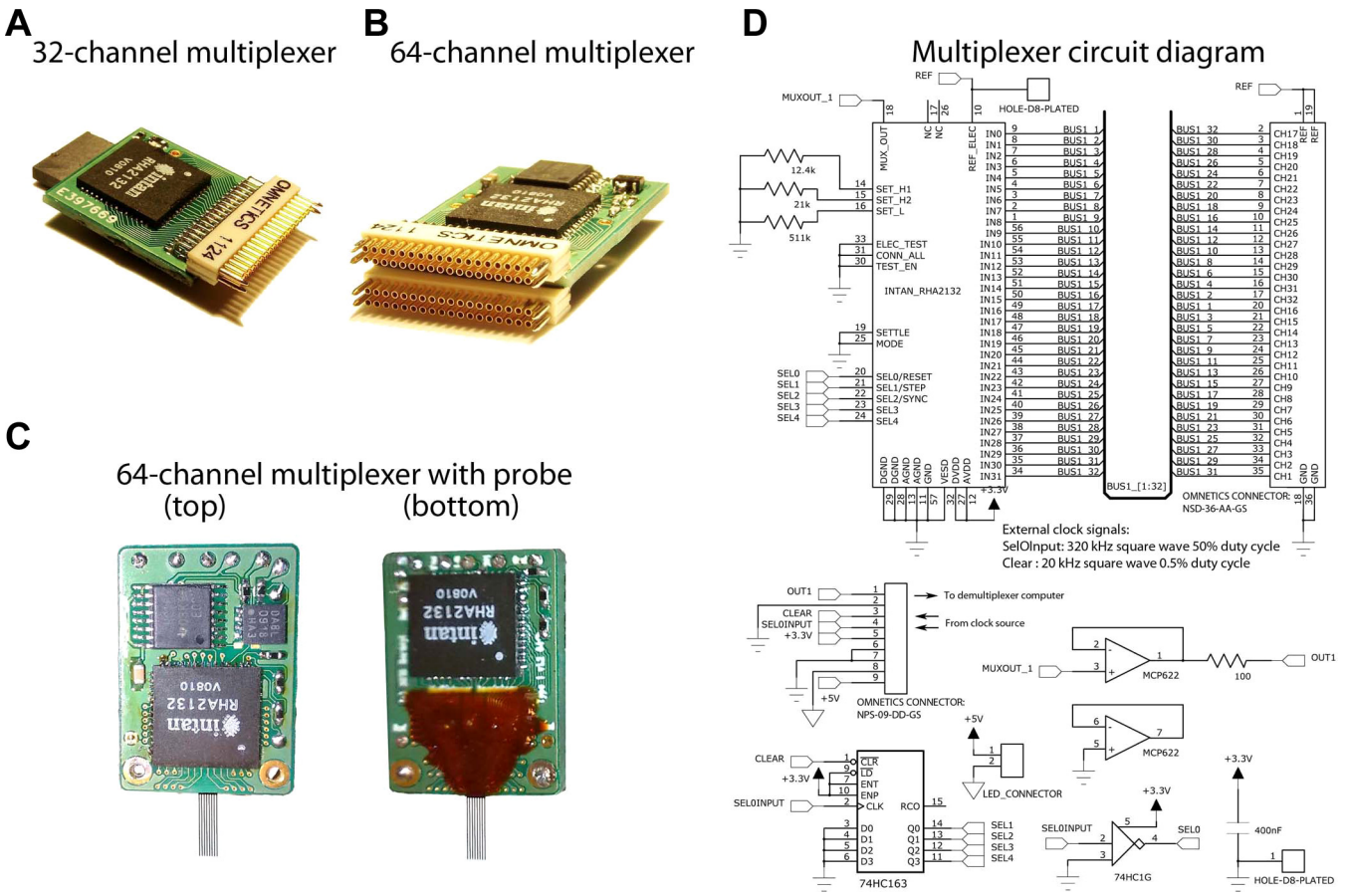

Fig. 3. Headstage multiplexers. *A* and *B*: 32- and 64-channel multiplexers with high-density Omnetics connectors. *C*: 64-site probe bonded to a 64-channel multiplexer. *D*: circuit schematics representing the electrical components and wiring scheme of the 32-channel multiplexer. *Top*: wiring diagram of the Intan RHA-2132 multiplexer chips and the high-density Omnetics connector for electrode interfacing. The cutoff frequencies of the low- and high-pass filters are set with the 3 resistors on the left. *Bottom*: supplementary electronics to provide clock bits and buffer the signal. Top row, left to right: 9-pin Omnetics connector interfaces with the main box; high-speed, dual-buffer operational amplifier. Bottom row: synchronous clock divider chip; external light-emitting diode (LED) power port for position tracking; clock inverter chip with Schmitt trigger; decoupling capacitor.

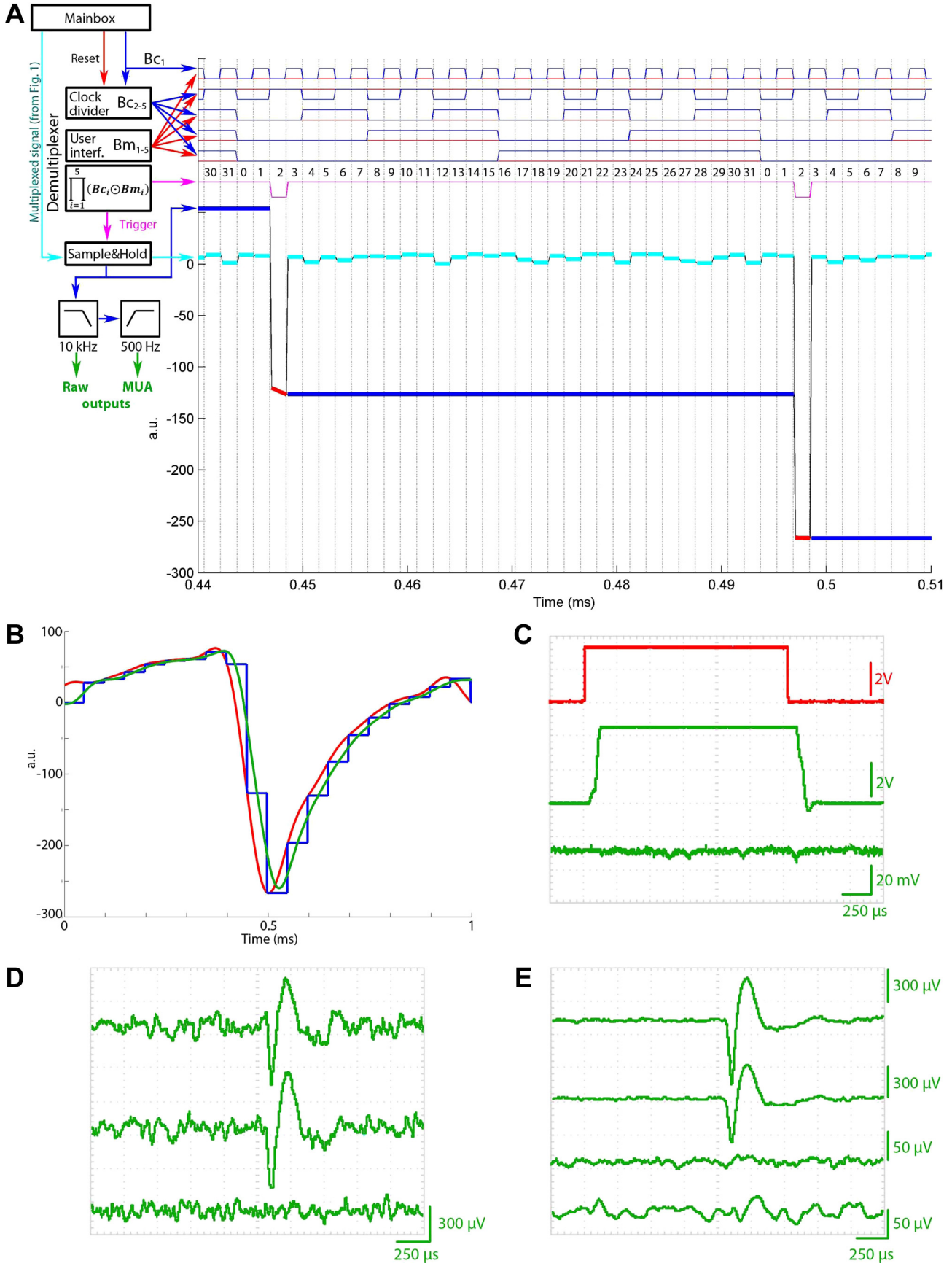

where MAP_{ij} is the transformed activity value of the *i*th shank and *j*th contact site to be displayed, LFP_{ij} is the filtered mean LFP value of a given channel, and *zf* is an arbitrary zooming factor. This transformation helped to visualize the smooth activity patterns while relatively suppressing the gross changes. The generated activity map (heat map) frames were further smoothed in space by cubic spline interpolation (10× upsampling) and in time by a 150-μs (3-sample) wide-moving average filter. A schematic of the anatomic layers was overlaid on each frame based on the histological verification of electrode location.

Mapping High-Frequency Power

The LFP signals were filtered by a narrow Gaussian band-pass filter (peaks at 300 Hz, SD = 10 Hz), and the power was summed up for 1-s-long periods. Several other high-passed signal bands (>300 Hz) provided similar results. In the hippocampus, the selected periods typically contained a sharp wave-ripple event to maximize the presence of unit firing since the goal was to identify the somatic layers. Several other frequency bands and bandwidths were tested, and the 300-Hz band was found empirically the most effective to outline the cell body layers (Ray and Maunsell 2011). This band was also less sensitive than higher frequencies due to the wide amplitude range of the isolated units that vary from site to site. The high-frequency power distribution effectively outlined the CA1 and CA3 pyramidal layers and the dentate area. In addition, the high-frequency power map agreed well with the locations of the clustered neurons. The predicted positions of the cell body layers were in good agreement with the anatomically reconstructed tracks of the probe shanks.

Coherence Analysis

Using coherence as similarity measure, an interaction energy-based clustering was implemented to identify cell layers. Every site served as a reference against all of the other referred sites. The resulting values were clustered using a gradient-descent algorithm so that each site was merged with that cluster for which the resulting coherence gain after merging was the largest. Starting from random initial assignments, the clustering algorithm formed stable but fewer clusters corresponding to a local energy minimum. Energy of *cluster A* is defined as:

$$E^A = \frac{-1}{N^A} \sum_{i,j \in A} C_{ij}$$

where C_{ij} is the coherence between *i*th and *j*th sites and N^A is the number of recording sites in *cluster A*. The energy gap between two different assignments to *clusters A* and *B* of *site i* is:

$$\Delta E_i^{AB} = \frac{1}{N^B} \sum_{j \in B} C_{ij} - \frac{1}{N^A} \sum_{k \in A} C_{ik}$$

If the energy gap is positive, *site i* moves into *cluster B*, otherwise it remains in *cluster A*. Since the method results only local minima of energy and stochastic components, such as the random initial condition and update order affects, clustering consistency was verified by repeating the process several times. Small (<3 sites in a cluster) and scattered clusters (typically representing bad channels) were deleted, and their sites were included into the majority cluster of their immediate neighborhood. This clarification was done either before or after merging the coherence clusters and multiunit activity (MUA) map. The resulting clusters effectively differentiated the different anatomic layers of the hippocampus (Fig. 5). The same coherence similarity method was used in the neocortex to differentiate the superficial, middle (layer IV), and deep layers of the neocortex (Fig. 8).

Merging the MUA and Coherence Cluster Maps

MUA map was thresholded at 70% of its maximum to define the cellular layers (CA1 and CA3 pyramidal and dentate gyrus granular). These sites were deleted from the coherence clusters to define new clusters. As a result, the CA1 and CA3 pyramidal layer and the granular layer became different clusters, designated as cell body layer clusters.

Coastline Display

In a different display, each site was connected to the most coherent sites on the neighboring shanks, which connected forward to the most coherent site of the next shank and so on. The recording positions were slightly and randomly scattered to assist visualizing the different lines crossing the same points. The connecting lines were colored on the basis of the cluster identity of their seed.

Estimation of Recording Quality and Comparison with a Commercially Available Nonmultiplexing Recording System

To obtain an objective measure of the recording quality of our multiplexing system, we performed the following analyses. The input-referred noise of the recording channels was measured by short-circuiting all inputs of the Intan chip (http://www.intantech.com) to the reference channel. The power spectrum of a 10-s-long recording was whitened after performing Fourier transformation. To evaluate the quality of recorded LFP and units, several consecutive, 10-min-long sessions (typically during immobility and sleep) were recorded from the hippocampus with a Buzsaki32 four-shank silicon probe (NeuroNexus). The recordings were made with either our multiplexed system (test) or a commercially available nonmultiplexed system (control) in an alternating sequence. The control system consisted of a headstage (gain = 20×; HST/32V-G20; Plexon, Dallas, TX) connected by a 40-wire Litz cable (same length as in the cable of the multiplexer) to a Digital Lynx 16SX analog-to-digital (A/D) converter (Neuralynx, Bozeman, MT). The multiplexed signals were sampled at 20 kS/s, whereas the Digital Lynx used 32 kS/s sampling. Pearson linear correlation was calculated across all combinations of channels (496 pairs) and visualized as a correlation matrix. A mean correlation

Fig. 4. Demultiplexer circuit. *A*: working principle of the real-time demultiplexer. The clock signal from the main box (Fig. 1) is successively halved 4 times to produce 4 subsequent clock bits (blue trace, $Bc_{1..5}$). A clock-bit-mask pattern set by the user interface (interf.; $Bm_{1..5}$, red traces) is pairwise-compared (XNORed) with the clock bits, and the results are logically ANDed. The output of this logical operation is the trigger (pink trace), which switches the sample-and-hold circuit so that when the clock bits match the preset mask the circuit works as a relay (1/32nd of the running cycle); otherwise, it holds the last sampled voltage (31/32nd of the running cycle). The output of the sample-and-hold circuit is shown as red and blue lines for the sampling and holding periods, respectively. The example demultiplexes channel 2. The demultiplexed signal trace is low-pass filtered to remove the step functions and optionally high-pass filtered at 500 Hz to separate unit firing from the local field potential (LFP). MUA, multiunit activity. *B*: temporal delay of the demultiplexing process. Red trace: original input waveform; blue trace: output of the sample-and-hold circuit; green trace: low-pass filtered signal at the output of the demultiplexer. *C*: signal transmission characteristics of the demultiplexer for a large-amplitude step function. Red trace: original input signal; upper green trace: demultiplexed waveform; lower green trace: demultiplexed signal on an adjacent channel in the multiplexed sequence. Note the different amplitude scales for the traces. *D*: single trace examples of a demultiplexed unit. The top 2 traces represent 2 waveforms representing 2 distinct projections of the spike onto 2 adjacent recording sites of the probe. The bottom trace shows the signal recorded on neighboring channel in the multiplexed stream. *E*: spike-triggered average waveforms of the neuron shown on *D*. Note the lack of cross talk in both the temporal (incomplete signal level settling during multiplexing or demultiplexing, 3rd trace) and spatial (cross talk across leads, 4th trace) domain.

value of the entire 10-min-long recording was calculated for channels on the same shank (within-shank correlation) and for channels located on different shanks (across-shank correlation). To estimate the contribution of higher-frequency components in the correlation, we repeated the analysis twice after passing the signals through a low-pass fourth-order Butterworth zero-phase lag digital filter (arbitrarily chosen 10- and 100-Hz cutoff frequencies, respectively). The raw recorded signals were processed to extract single-unit spike trains and clustered automatically by the KlustaKwik program (Harris et al. 2000). To avoid subjectivity, the manual cluster refinement step was limited to eliminate the obvious noise clusters (waveforms with same amplitude and shape on every recording site of the given shank). The number and quality of the isolated single units were assessed using the following three criteria. In the first analysis, the number of automatically isolated non-noise clusters was compared disregarding their isolation quality. In the second comparison, we measured the ratio of the number of isolated spikes and the number of noise waveforms to estimate the signal-to-noise ratio. Third, we used two levels of cluster quality measures (permissive and conservative; see above). The recorded waveforms of identical spike clusters recorded by the two systems were also compared after amplitude normalization and offline interpolation (upsampling) to 50 kS/s.

RESULTS

System Description

Large-scale recordings from multiple single units, large spatial coverage, and limited tissue displacement/damage by the electrodes are competing conditions (Buzsáki 2004; Du et al. 2011). Our goal was to monitor single-unit and LFP activity patterns of neighboring neocortical regions and interconnected hippocampal subregions. To this end, we designed an 8-shank probe with 32 recording sites on each shank (Fig. 1*A*). The recording sites are arranged vertically at 50-μm steps, providing sufficient spatial resolution for unit clustering (Csicsvari et al. 2003; Montgomery et al. 2008; Wilson and McNaughton 1993) yet large vertical coverage (1,550 μm). Each recording site is 165 μm^2 and has an impedance between 1.3 and 3 MΩ. The shanks are placed 300 μm apart to eliminate simultaneous recording of neurons by adjacent shanks (Henze et al. 2000) and provide spatial coverage of adjacent neocortical modules or hippocampal regions (Csicsvari et al. 2003). Each shank is 15 μm thick and tapered from a sharp tip to 96 μm at the uppermost recording site to minimize tissue damage yet rigid enough to allow smooth penetration through brain tissue. The total volume of the probe shank, containing the recording sites, is comparable with traditional wire tetrodes (Wilson and McNaughton 1993). In contrast to the blunt tetrode, which often tears intracortical blood vessels during penetration, the tapered profile of the silicon probe shanks allows it to be moved up and down in the brain with continued yield of units. The probe is connected to a microdrive so that the probe sites can be advanced to the vicinity of the desired neurons (Vandecasteele et al. 2012; Fig. 2).

Signal multiplexing and processing. A major challenge of the effective use of silicon probes in small animals is to reduce the volume and weight of the instrumentation between the probe and the recording equipment. Multiple connectors, traditional preamplifiers and multistrand cables for each recording site are not viable for high-density probes; the large volume and weight of these components and the increased tension of the connecting cable significantly limit the behavior of the small rodent. In addition, using large numbers of individual external amplifiers is prohibitively costly and involves complex cabling. A logical solution to these problems is the deployment of time-division multiplexing (Harrison 2008; Olsson et al. 2005; Szuts et al. 2011; Viventi et al. 2011). To this end, we used 32-channel VLSI analog signal multiplexers developed specifically for brain recording applications (Harrison 2008; RHA2132; Intan). Eight multiplexers are soldered to a custom-designed printed circuit board, four on each side (Fig. 1*A*), to transmit a total number of 256 channels. To allow movement of the probe and preserve its small inertia, an ultraflexible polyimide-based cable was designed and served as an interconnect between the probe and the multiplexing headstage (Fig. 1*A*).

Each of the 256 electrical signals acquired by the silicon probe is amplified and band-pass filtered (gain = 200×, cutoff frequencies of the high-pass and low-pass filters are 0.3 Hz, −6 dB/octave and 10 kHz, −18 dB/octave, respectively; Fig. 1*B*). The broadly tuned cutoff frequencies allow the recording of broad-band signals (LFP and unit activity simultaneously) from all recording sites. The signal multiplexer chips were programmed to switch sequentially between channels every 1.5 μs so that a sweep of 32 channels corresponds to 48 μs (Fig. 1, *C* and *D*). To accomplish a 50-μs cycle length (20 complete scan cycles in a millisecond), the last channel of the 32-channel block was transmitted for 2 ms more before looping back to the 1st channel of the subsequent cycle. The postloop 2-μs time was used to protect against desynchronization of the multiplexing sequence. Potential desynchronization of the multiplexing and demultiplexing sequence may occur if the clock signal accidentally advances the sequence of the multiplexed signal. Such accidental "jumps" are avoided by resetting the binary counters to zero (binary code 00000) during the 2-μs postloop time. This clock supervision mechanism ensured that even if the clock code is corrupted for any reason, only 1 sample is misplaced in the sequence of the parallel-decoded channels. To reduce the wiring complexity of the printed circuit board interconnects, the 32 recording sites of a given shank did not correspond to a single multiplexer but were distributed among at least 4 chips. This had the added value that in case of a chip failure some recordings from all shanks remained available.

We found that the relatively high output impedance of the RHA2132 multiplexer chip was not sufficient to transmit signals reliably over long data cables (>5 m), typically needed in behaving experiments. To improve signal settling time and to circumvent the capacitive load of the cable, high-precision operation amplifiers (MCP622; Microchip; slew rate: 27 V/μs; Fig. 3*D*) were added in series to buffer the multiplexed signals. With the added buffering, the signal settled in <100 ns to 1% precision after each switch of the multiplexer chip even when up to 15-m-long cable, consisting of 36-gauge (110-μm) Litz wires, was used. The ultralight and ultraflexible cable allowed for a free movement of the animal (Vandecasteele et al. 2012; Fig. 2*F*).

To achieve synchronous channel advancement on every multiplexer chip without adding further weight and surface area to the headstage, the common clock signal (640 kHz, 50% duty cycle) is generated by a programmable integrated circuit in the external controller box ("main box"). A 5-bit binary clock code was generated by a synchronous binary counter (74HC163; Texas Instruments) on the headstage to address the channels of the multiplexers within blocks of 32. In the main

box, the multiplexed signals were further amplified (gain = 2, total gain = 400), and their baseline was corrected by the subtraction of a preset voltage value. The multiplexed signals (Fig. 1, *C* and *D*) were sampled by a high-speed digital-to-analog converter (PCI-6133; National Instruments). Sampling was initiated by the clock generator microchip of the main box 125 ns before the subsequent channel switch to exploit the available signal settling time maximally.

Software control. To generate the clock and trigger signals, the programmable integrated circuit was activated by the re-

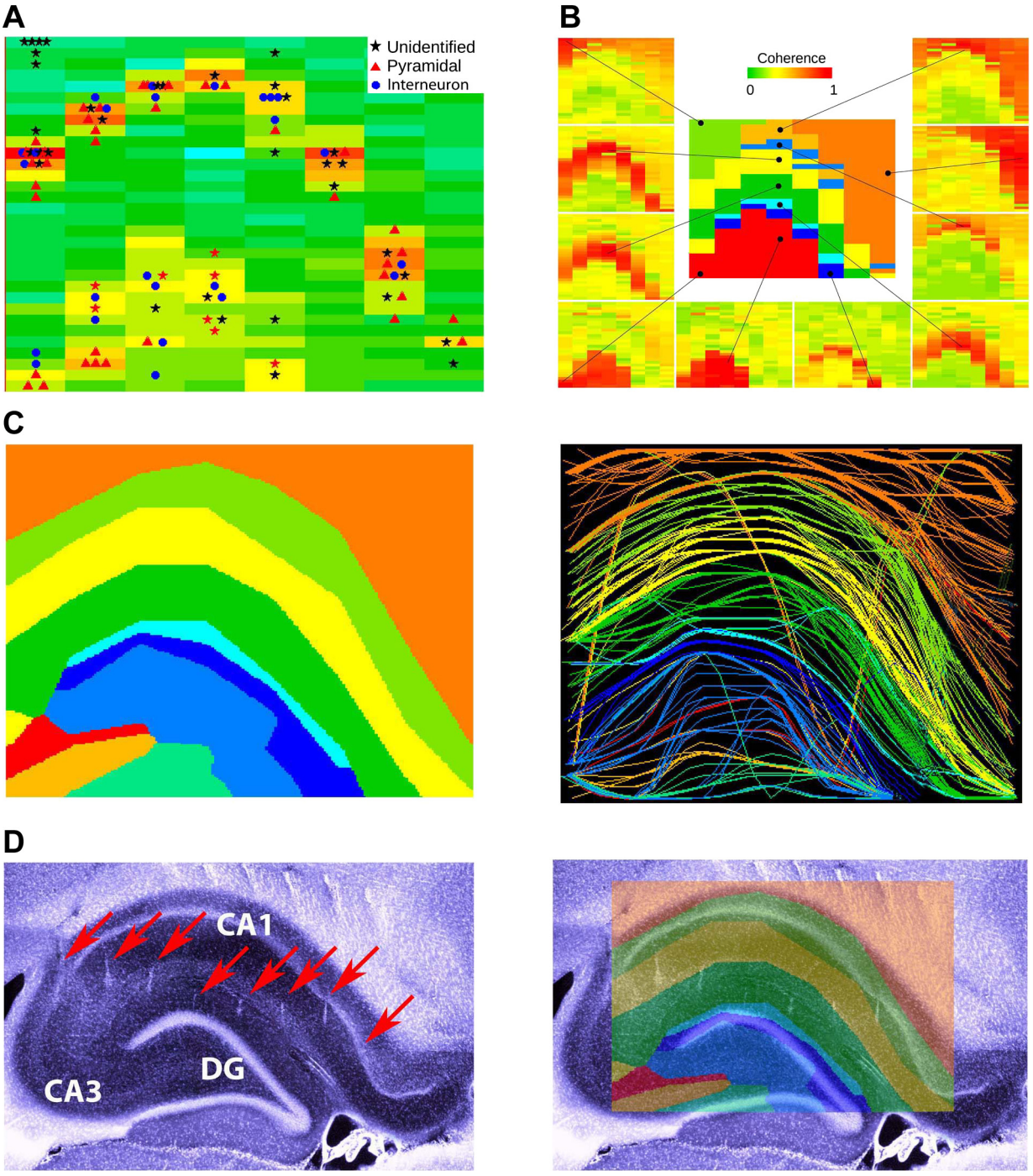

Fig. 5. Electroanatomy of the hippocampus. *A*: distribution of high-frequency power (300 ± 10 Hz) on each of the 256 sites of the silicon probe. The 32 × 8 color matrix is a representation of the 256-site probe shown in Fig. 1*A*. Each rectangle represents a 300-μm (intershank distance) by 50-μm (vertical intersite distance) area to mimic the 2-dimensional geometry of the probe coverage. Clustered neurons, assigned to the largest amplitude recording sites, are superimposed on the power map. *B*: coherence maps of gamma activity (30–90 Hz). The 10 example sites (black dots) served as reference sites, and coherence was calculated between the reference site and the remaining 255 locations for a 1-s long recording segment (Fig. 7). *C*: composite figure of the combined coherence maps (see also Fig. 7). *Left*: 2-dimensional combined map of gamma coherence and high-frequency power distribution. Right: coastline map of layer-specific coherence contours. *D*: histological reconstruction of the recording tracks (arrows). The shifting of the tracks in the neocortex is due to a slight displacement of the neocortex/corpus callosum relative to the hippocampus during the tissue sectioning process. DG, dentate gyrus. Right: physiology-based map superimposed on the recording tracks.

cording software only after the digital-analog data acquisition (DAQ) task was properly set up and was idle for the external trigger to start sampling. The recording software program acquired samples from the buffer in chunks of 100 ms (100 ms × 20 samples per millisecond × 32 channels = 64,000 samples per multiplexed line). This 100-ms (10-Hz) readout frequency offered a practical compromise between minimizing the time requirement introduced by the frequent updates of the processing code headers yet provided a smooth, real-time-like data display on the computer screen. After the buffer was filled, the acquired data were read out by the recording software and reordered to a 32 × 2,000 size matrix. The synchronous initiation of the sampling and clock advancement ensured that the data set of each buffer readout started with a sample corresponding to the first channel on the input side of the multiplexer chip (Fig. 1*D*). Although the actual clock code of the software and the hardware were not synchronized after the initiation, we never experienced any misalignment of the channel order even after extended testing of the entire system up to 40 kS/s sampling speed per channel. The electrophysiological recording setup was combined with a universal serial bus (USB) Web camera recording system for the continuous monitoring of the animal's position and behavior (Figs. 2 and 3).

Real-time hardware demultiplexing. Many applications need not only recording of the neuronal signal, but also its real-time availability, e.g., to interact with brain circuits in close-loop experiments (Berényi et al. 2012; Stark et al. 2012). However, the content of the buffer of the analog-digital card is read only once every 100 ms, and the software routines introduced between an analog-digital and digital-analog conversion per se provide a suboptimal time precision for brain feedback stimulation. To achieve real-time readout (<50 μs per sample), we designed a mixed analog/digital demultiplexing device (Fig. 4). The demultiplexer, in addition to receiving analog data streams, was timed by the same clock signal that drove the headstages, and the rest of the clock bits were generated by the principle as described above for the multiplexers. Two separate bit-masks (2- and 3-bit) were generated by a microcontroller-driven user interface that allowed the selection of any one of the 8 multiplexed streams (using an analog switch circuit) and any of the desired channels of the selected stream (1 of 32). Demultiplexing was established by a pattern-matching algorithm: the real 5-bit clock signal was compared with the user-preset clock bit mask by a series of XNOR and AND logic gates. The digital output of the circuit generated a digital high level only if the clock mask matched the real clock signal (i.e., approximately the duration of the segment of the desired channel within the multiplexed stream). In principle, this digital pulse was suitable to trigger the sampling mode (i.e., a voltage follower) of a sample-and-hold integrated circuit, which worked as a voltage follower. The falling edge of the trigger pulse switched the sample-and-hold circuit to hold the last voltage value until the next sampling cycle, thus bridging the time gap, whereas the consecutive channels were transmitted in the multiplexer line (Fig. 4*A*). Because the propagation time of the digital gates introduced a significant delay in the digital trigger pulse, it could not be used directly to trigger the sample-and-hold circuit. To correct for the delay, a monostable multivibrator ("one shot") was used to generate a shorter pulse (1.3 μs) so that the sampling was terminated before switching to the subsequent sample in the multiplexer line. The output of the sample-and-hold circuit was then low-pass filtered (at 10 kHz) to eliminate the

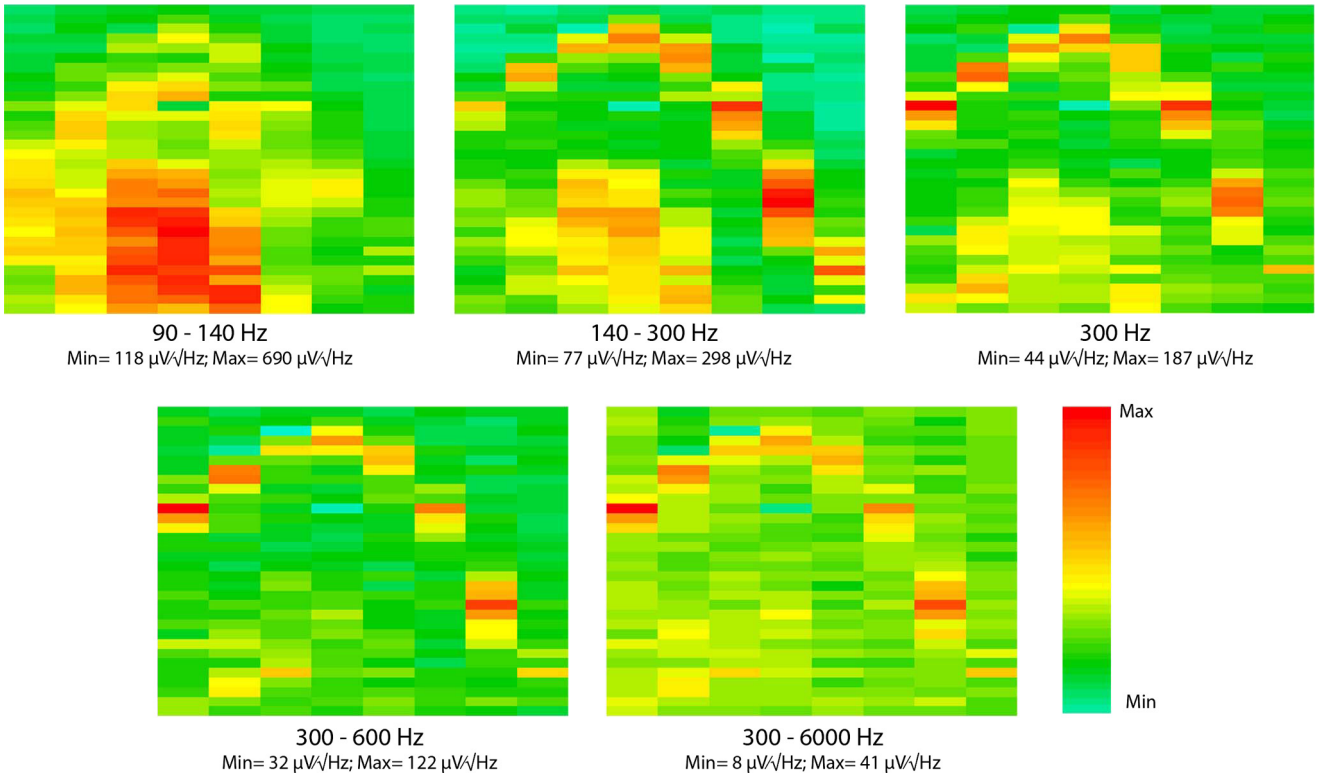

Fig. 6. Layer-specific LFP power distribution of various frequency bands in the hippocampus. The arrangement of each panel is the same as Fig. 3*A*. Each panel is showing the power map of the same representative, 1-s-long recording segment containing sharp wave-ripples (SWR). For details on filtering, see MATERIALS AND METHODS. Min, minimum; Max, maximum.

step responses (Fig. 4*B*). The reconstructed analog signal was amplified or filtered further as required for audio-monitoring the recorded signal or viewing the waveform on an oscilloscope (0.5 Hz to 5 kHz; Fig. 4, *D* and *E*).

Physical dimensions. To eliminate complex cabling and connections of high-channel counts of the probe, the probe was permanently connected to the 256-channel multiplexer headstage (4.7 g; 34 × 39 × 2.5 mm) and is worn chronically by the rat. During recording, the animal was connected to the recording system through an ultraflexible cable (Vandecasteele et al. 2012; 12 127-μm-diameter insulated copper wires, 455-μm-total-diameter cable; Fig. 2*F*). For recording from smaller-sized silicon probes or tetrodes targeting multiple brain structures, we constructed 32- and 64-channel versions of the multiplexer headstage (32-channel: 0.9 g; 13 × 15 × 3 mm; 64-channel: 1.2 g; 13 × 19 × 3 mm, respectively; Fig. 3). In contrast to the 256-channel version, the front ends of these headstages were connected to the probe output by high-density connectors (Omnetics) during the experiments.

Validation of the recording system and estimation of the signal quality. We estimated the mean input referred noise spectrum for all channels of the 32-channel multiplexer headstage (the results presented here apply to the 64- and 256-channel headstages as well since they consist of parallel-connected 32-channel blocks). When the input channels were short-circuited with the reference pin of the headstage, the mean root-mean-square amplitude of 60-Hz noise was 7.2 μV (range = 2–8.5 μV), which is approximately one order of magnitude higher than the half least significant bit of the A/D conversion. We also compared the signal quality with a commercially available recording system (HST/32V-G20 preamplifier; Plexon) and Digital Lynx 16SX A/D converter (Neuralynx). The amplitude of the signal was ~20% smaller using the Intan amplifier chips than that of the nonmultiplexing control system, which can be explained by the lower input impedance of these chips. However, the signal waveforms and the wave shapes of the extracellular spikes were virtually identical. The mean difference between the normalized spike waveforms of a well-isolated test single unit, recorded by the current and the control system, was 10% of the standard deviation of the waveform recorded by the control system. The common noise component across channels in the recorded LFPs was significantly lower, especially in the lower frequency ranges, which is presumably a result of the serial transmission of the channels in the multiplexed line instead of the nonmultiplexed parallel transmission. The intrashank correlation of the recorded signals (i.e., the mean of the correlation values calculated between pairs located on the same shanks; see MATERIALS AND METHODS) was similar in both systems for every investigated frequency range. However, the mean correlation across the shanks gradually decreased at higher frequencies in our system (r = 0.8, 0.72, and 0.23 for >1, >10, and >100 Hz, respectively) while slightly increased for the control system (r = 0.55, 0.72, and 0.75). The single-unit yield was larger in our system despite the slightly lower signal amplitude and lower sampling rate (20 vs. 34 kS/s). After the automatic spike

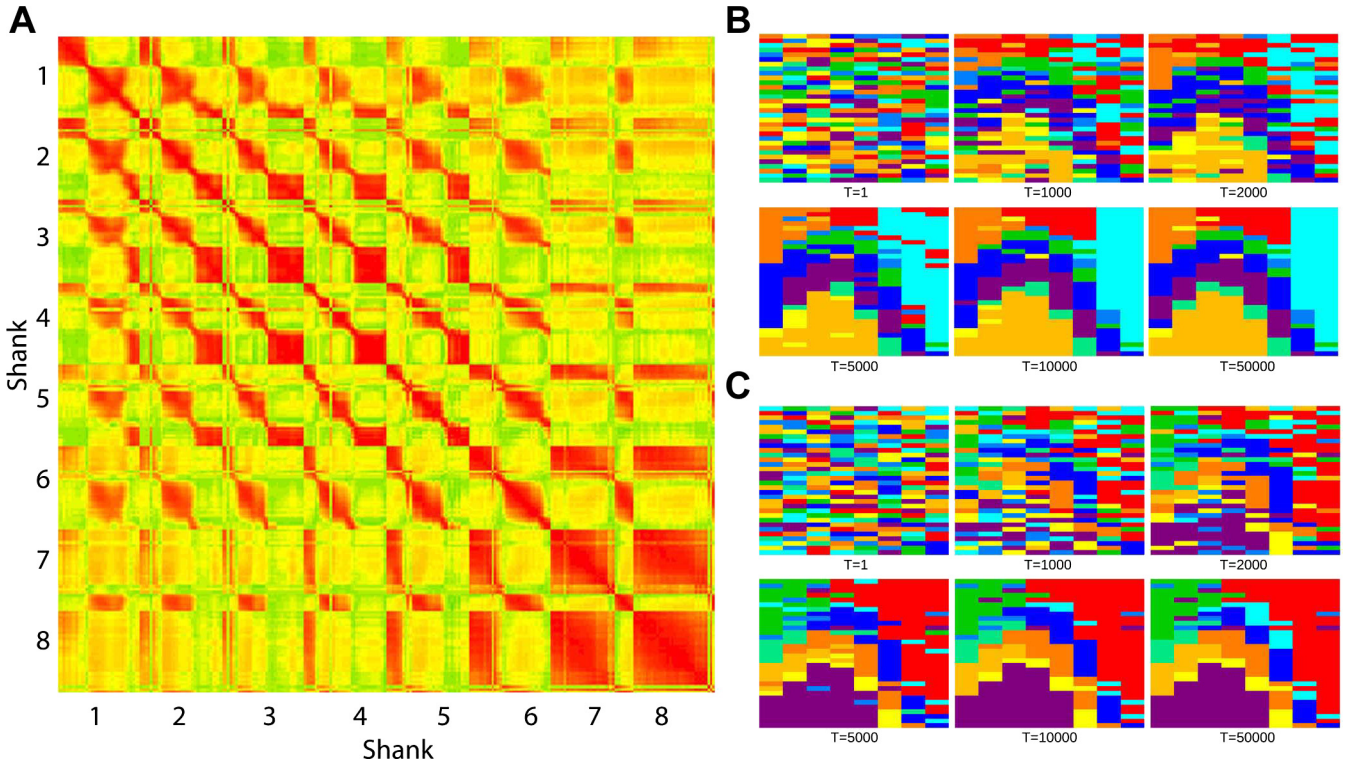

Fig. 7. Coherence-based clustering of electrode sites. *A*: cross-coherence-matrix of the recorded 256 channels calculated from a randomly selected, 1-s long recording segment. *B* and *C*: evolution of coherence clusters during clustering procedure. Initially (T = 1, with T denoting the number of algorithmic steps), electrode sites, represented by rectangles, distributed randomly among 10 clusters denoted by different colors of the rectangles. During each step, the algorithm examines whether reassignment of 1 randomly chosen electrode site into another randomly chosen cluster would increase the mean coherence of the cluster. If it does, the site is merged into the cluster. During the iterative reassignments, clusters emerge and stabilize. Stability is shown by the negligible changes between 10,000 and 40,000 iterations. *B* represents the clustering for a sleep session (sharp-wave event), whereas *C* is created from a random sample during exploratory behavior (theta).

extraction and clustering of the sample session recorded by both systems (see MATERIALS AND METHODS), 26 and 7 single units were detected on a single shank using our (test) and the control systems, respectively. After taking account of cluster quality criteria, nine vs. five clusters, respectively, satisfied our conservative criteria (see MATERIALS AND METHODS).

Physiological Recordings

Electroanatomy of cortical layers. We have implanted the high-density, 256-site probes in 5 rats. In 2 rats, 2 probes were implanted (512 channels). In 1 rat the probes were placed in the same hemisphere, whereas in the other animal they were placed symmetrically in the 2 hemispheres (Fig. 2).

The relationship between laminar arrangement of afferents and the characteristic depth profiles of various oscillatory and irregular LFP patterns can offer means for an identification of the various cortical layers and their transitions (Buzsáki et al. 2012; Montgomery et al. 2008). Here, we illustrate our strategy in the hippocampus, for which laminar structures and well-understood LFP patterns allow for an online quantitative identification of each of the recording electrode sites (Montgomery et al. 2008).

First, each of the 256 LFP signals was filtered by a narrow Gaussian band-pass filter (peak = 300 Hz, SD = 10 Hz), and power values, determined from a randomly sampled 1-s epoch, are displayed for each of the 256 sites as a 2-D map (Fig. 5*A*). This frequency band was empirically determined by selecting a frequency band with the largest ratio of power between cell body layers and dendritic layers (Fig. 6). The band we selected (300-Hz Gaussian filter, SD = 10 Hz) presumably represents various aspects of MUA (Ray and Maunsell 2011) since its spatial distribution clearly marked the pyramidal layer and the dentate-hilar area, as reflected by the density of the recorded units. The soma location of the recorded neurons was estimated by the largest amplitude waveform representing the firing of each unit (Csicsvari et al. 2003; Fujisawa et al. 2008) and assigned to the recording site of the relevant shank in the electroanatomic map (Fig. 5*A*). In the next step, coherence maps in the gamma frequency band (40–90 Hz) were constructed. Each site served as a reference, and coherence distribution with each of the remaining 255 sites was determined iteratively (Montgomery et al. 2008; Figs. 5*B* and 7*A*). Using a gradient-descent algorithm (Fig. 7), the recording sites were clustered based on the resulting coherence matrix, and the resulting coherent channels were grouped together. Next, a 2-D gamma coherence map was generated (based on the spatial locations of the recording sites and their coherence cluster identities) and combined with the power map (Fig. 5*C*) to identify the cellular layer among the emerging clusters. The boundaries of the channel clusters happened to be nicely overlapping with the anatomic layers without any a priori knowledge of the histological control. In a different display, each recording site was connected to its most coherent neighbor on the adjacent shanks. The connecting lines were color-coded on the basis of cluster identity of their leftmost member site. The resulting coastline display provided a smooth, layer-specific map of the recorded space by the silicon probe (Fig. 5*C*, *right*). The electroanatomic map constructed from unit firing and LFP signals corresponded faithfully to the histological reconstruction of the electrode tracks and the anatomic layers of the hippocampus (Fig. 5*D*).

High-density silicon probe recordings in the neocortex were similarly advantageous for cortical layer identification. Gamma coherence reliably identified three separate layers, corresponding to the superficial (II/III), middle (IV), and deep (V/VI) layers (Fig. 8*A*).

Large-scale recording of unit activity. Figure 8*B* shows wide-band (0.5 Hz to 10 kHz) traces from a single shank in the somatosensory cortex. Neurons were recorded from all shanks of the probes in both hemispheres for several days before advancing the probes into the hippocampus. In conjunction with LFP, population patterns of unit firing allowed for a clear classification of brain states (Fig. 8*C*).

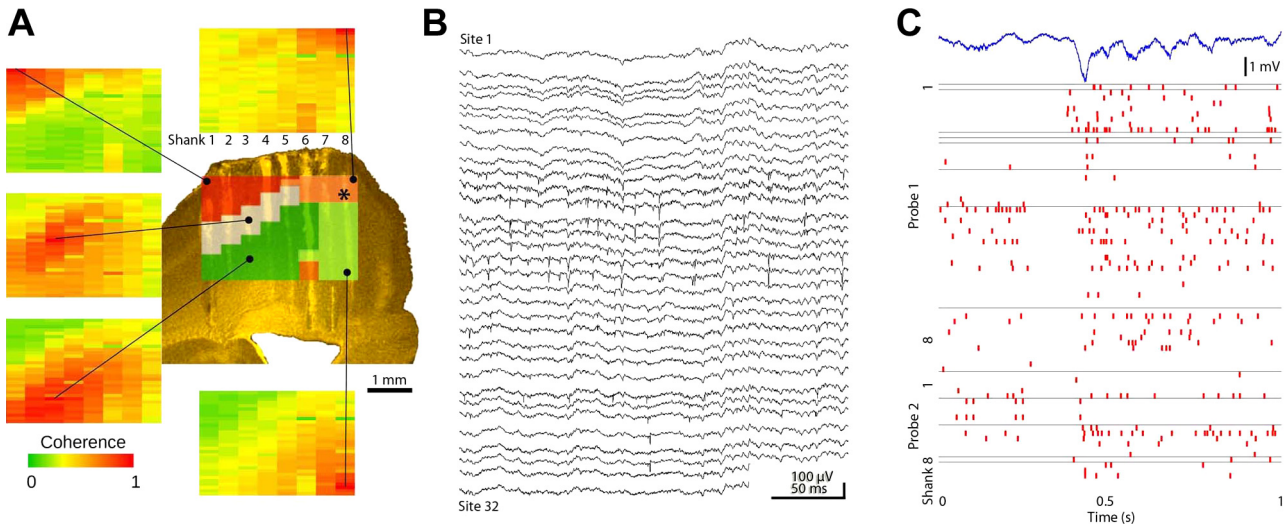

Fig. 8. Electroanatomy of the neocortex. *A*: combined coherence map of gamma activity (30–90 Hz) as in Fig. 5*B*. Each site served as a reference, and coherence was calculated between the reference site and the remaining 255 locations. The resulting combined map is superimposed on the histologically reconstructed tracks in the sensorimotor cortex. Note reliable separation of layer IV, superficial, and deep layers and the lack of a layer IV coherence band in the adjacent motor cortex (*shanks 6-8*). *B*: 300-ms-long raw signal traces of a shank spanning across multiple layers of the cortex showing spike activity of multiple neurons. *C*: relationship between the activity patterns of multiple neurons and the LFP during a sleep spindle episode. The recording site of the LFP trace in marked by an asterisk on the top of the panel in *A*. The figure is a representative sample for illustration purposes only.

Neocortical and hippocampal units were clustered semiautomatically (Harris et al. 2000) followed by physiological classification of the units into putative principal cells and interneurons (Barthó et al. 2004; Fujisawa et al. 2008). To obtain "at glance" information about the recorded neurons, an algorithm was designed to summarize the main physiological and behavioral correlates of each unit (Fig. 9). First, the mean waveform of the unit recorded at multiple sites is displayed together with wave-shape classification of the unit and its autocorrelogram and ISI histogram. The next level of analysis characterizes the spike-LFP relationships. In case of hippocampal neurons, the preferred firing phase in relation to theta, gamma, and ripple oscillations of the unit are displayed together with sharp-wave-related firing (Fig. 9). The third level of analysis shows the behavioral correlates of the neuron such as its place-related firing in the maze and spike-phase precession relative to the theta rhythm (Fig. 9). The display panels can be flexibly replaced with other analyses such as displaying the anatomic location of the neuron in 2-D space, its cluster space relative to surrounding clusters, brain-state dependence of firing rates, and cross-correlation with selected other neurons.

The 256-site probe was designed for large spatial coverage to allow monitoring the activity in multiple hippocampal layers. This inevitably compromised the density of the recording sites (50 μm) and, consequently, reduced the unit clusters with high isolation quality (MATERIALS AND METHODS) compared with higher-density (20-μm spacing) probes. However, the lower unit yield per site was offset by the ability of the 256-site probe to record from multiple layers (Fig. 10).

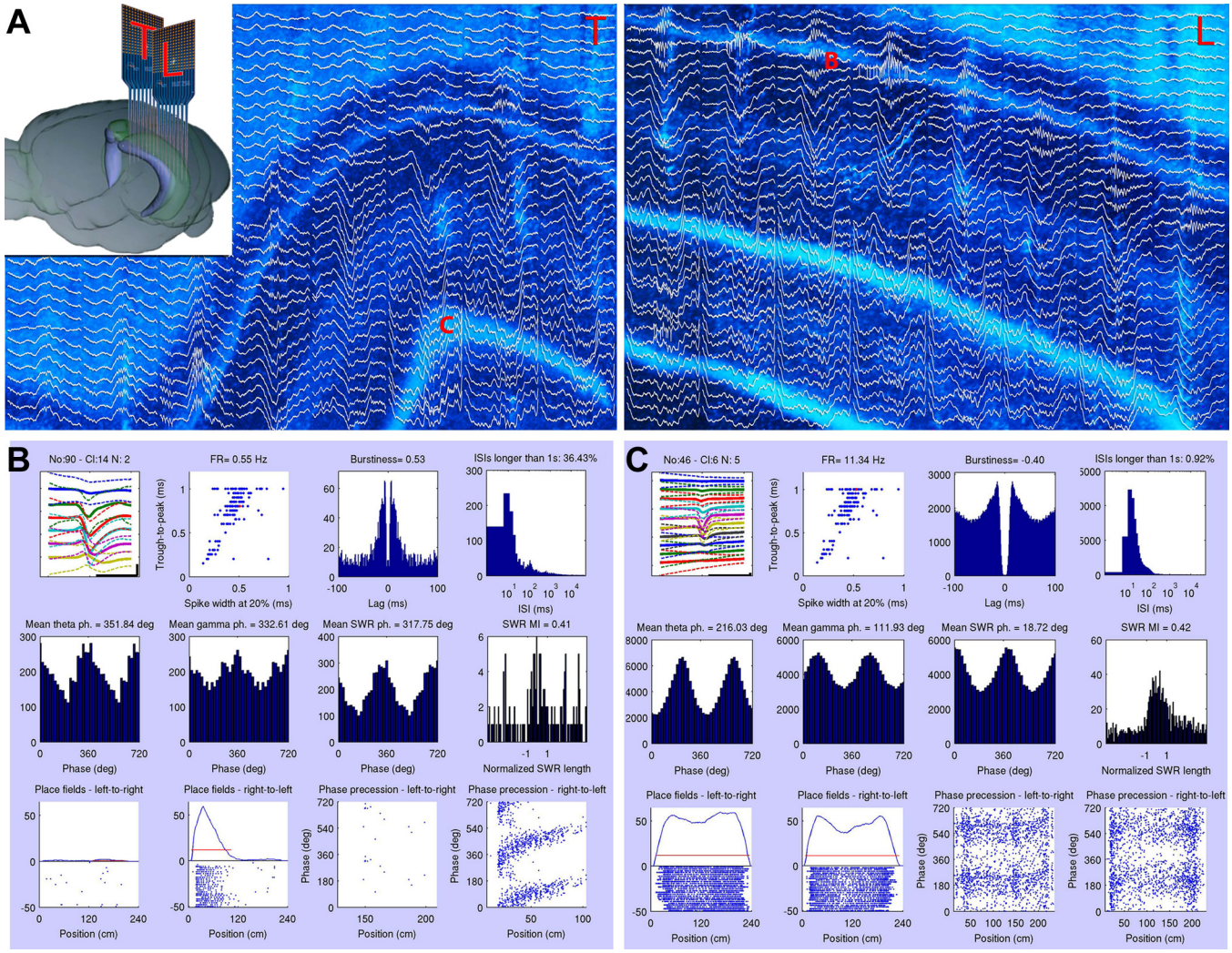

Fig. 9. Characterization of single units. *A*: orientation of 2 probes placed in the same hippocampus in the transversal (T) and longitudinal (L) axes (see also Fig. 2*A*). Histological reconstruction of the recording probe shanks with superimposed traces of a SWR event (300 ms). The tissue slices were cut parallel with the probe shanks, i.e., perpendicular and parallel with the longitudinal axis of the hippocampus. "B" and "C" mark the anatomic locations of the 2 recorded example neurons presented in *B* and *C*. *B*: characterization of 2 different units recorded from the sites marked by "B" and "C" in *A*. First row of each panel shows: *1*) 2-ms traces of a hippocampal single unit recorded from multiple sites of the shank. The label above the plot denotes the recorded neurons identifier; *2*) classification of unit clusters, recorded in a single session, on the basis of their trough-to-peak duration vs. spike width at 20% of the trough magnitude. The relevant unit is indicated by a red dot; *3*) autocorrelogram and burstiness index determined as the ratio of spikes at <8-ms intervals divided by all spikes (Mizuseki et al. 2009); and *4*) interspike interval (ISI) histogram (log scale). Second row: cross-correlation between LFP and unit firing showing separately for theta (4–12 Hz), gamma (30–90 Hz), and SWR (120–250 Hz). Preferred phase (ph.) of firing is also shown numerically. *Phase 0* corresponds to through. Last panel: SWR-related firing of the unit. The duration of the SWR is normalized. The modulation index (MI), defined by difference/sum of the firing rate (FR) during and outside of ripples, is shown above the panel. Third row: position-dependent firing rates ("place cell" activity) during left and right journeys in the maze and corresponding spike-phase relationship to position within the largest place field (red lines). deg, Degrees.

Large-scale recording from local circuits has the power of identifying monosynaptic connections at least between principal cells and interneurons (Fujisawa et al. 2008). This is typically done by examining counts of cooccurrences of spiking in the putative pre- and postsynaptic neurons as exemplified by the large peaks at short-latency time lags (Fig. 11, *A* and *B*). Our analysis is limited only to pyramidal-interneuron interactions since the validation of the monosynaptic peaks on the cross-correlograms of the pyramidal-pyramidal neuron pairs was not reliable due to their low firing rates. However, with extended recordings and increased number of spikes, the circuit analysis can be extended to pyramidal-pyramidal connections as well (Hirabayashi et al. 2013). Of the 26,406 possible connections of a total of 163 simultaneously recorded neurons (counting each literal pair twice, corresponding to the 2 directions) recorded by 2 probes (512 sites) in the same hippocampus (Fig. 11, *A* and *B*), 137 pairs (0.005%; Fig. 11*C*) had short latency (<5-ms onset) and narrow significant peaks (<2 ms) or troughs in their cross-correlograms, indicating that the presynaptic partner neuron was an excitatory or inhibitory neuron, respectively. In most cases, the postsynaptic targets were interneurons, as judged by their high firing rates and waveforms (Sirota et al. 2008). Most functionally connected pairs were detected locally in the same hippocampal region, but several connections were detected between neurons in the CA3 and CA1 regions as well (Fig. 11). Several pyramidal cells of both local and distant origin could converge on the same putative interneuron.

Increasingly larger numbers of simultaneously recorded neurons also facilitate the search for spatiotemporal patterns of neuron interactions in local circuits because the likelihood of finding connected pairs increases quadratically with the number of the recorded cells (Barthó et al. 2004; Carandini 2012). Since the spike transmission probability (i.e., the excess numbers of postsynaptic spikes divided by the number of presynaptic spikes, reflecting the efficacy of spike transfer function) can be used as an indirect measure of synaptic strengths between neurons (Fujisawa et al. 2008), the magnitude of spike transfer can be used in future studies to estimate the state- and task-related circuit reconfigurations (Fujisawa et al. 2008).

State-dependent activation of single neurons by multiple inputs. In the intact brain, neurons are embedded in interconnected networks and respond with spikes to a single input or a combination of inputs. Since afferents to hippocampal neurons target specific layers, high-density recordings from multiple layers and regions can, in principle, track the activity of the afferents giving rise to each spike. To illustrate the principle, we sampled LFP multiple times at all recording sites in 20-ms windows, centered on the spikes of a CA1 pyramidal neuron during sharp wave-ripple events and ambulation while the rat was walking through the place field of the neuron (O'Keefe and Nadel 1978; Fig. 12; Supplemental Video S1, available in the data supplement online at the *Journal of Neurophysiology*

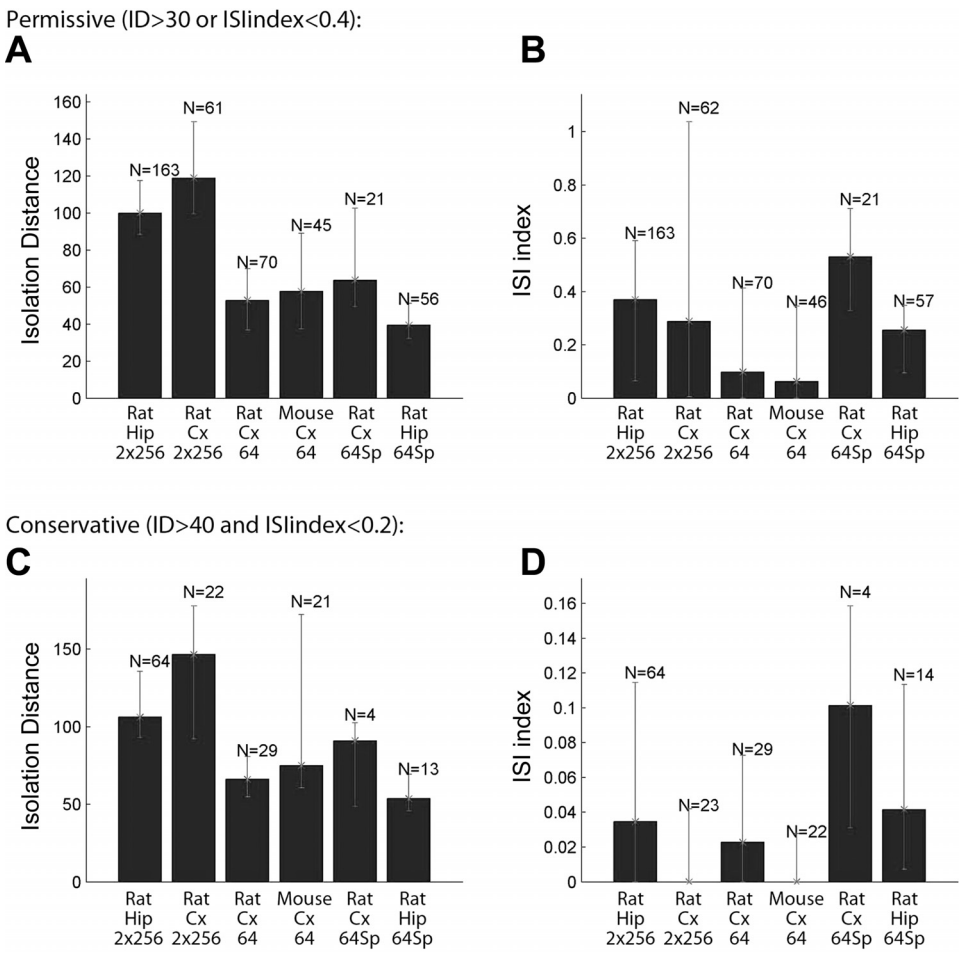

Fig. 10. Comparison of single-unit isolation metrics. Each measure is shown for 6 different recording conditions (probe, structure, and species). *A* and *C*: Mahalanobis distance of isolated spike clusters in high-dimensional feature space. *B* and *D*: contamination of isolated single-unit clusters calculated as the ratio of spikes occurring within (2 ms) and after (20 ms) the refractory period of the given neuron. Medians and the interquartile ranges are shown. N denotes the number of neurons fulfilling the inclusion criteria. *A–D* display the same data set using permissive and conservative inclusion criteria, respectively. ID, isolation distance; Hip, hippocampus; Cx, cortex; 2 × 256, 2 256-channel silicon probes with multiplexing headstages; 64, Buz64-type silicon probe with 20-μm intersite distance with multiplexing headstage; 64Sp, Buz64Sp-type, 6-shank silicon probe with 20-μm intersite distance equipped with an optical fiber on each shank recorded by a nonmultiplexing headstage and amplifier.

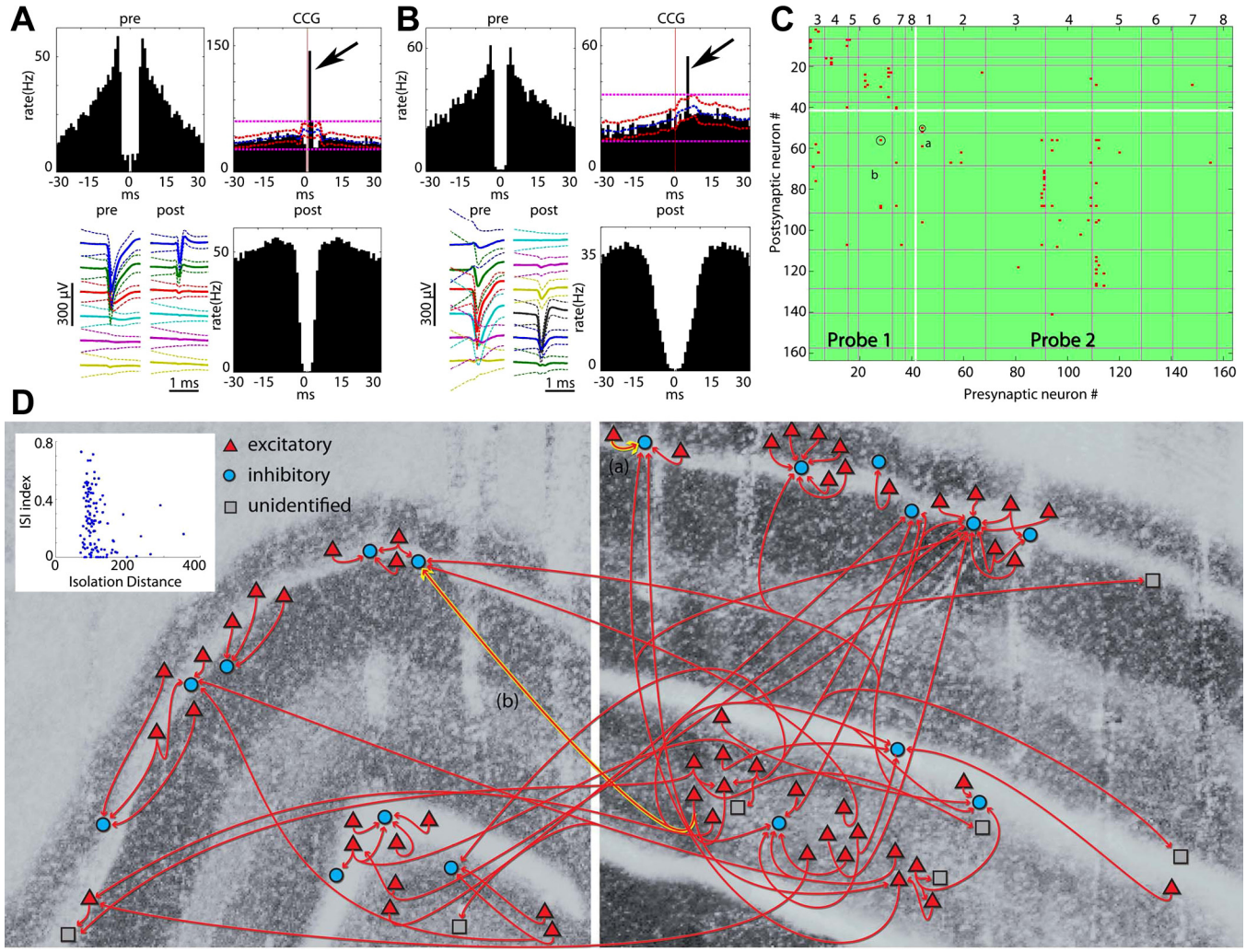

Fig. 11. Partial circuit reconstruction from physiological interactions. *A*: identification of monosynaptic connections. Only pyramidal-interneuron connections are shown. Autocorrelogram of the reference (presynaptic) neuron (pre), referred (postsynaptic) neuron (post), and cross-correlogram (CCG) between the neuron pair. Short-latency (<1 ms) narrow peak (arrow) identifies the reference cell as a putative excitatory (pyramidal) neuron. Blue line, mean of time-jittered spikes; red line, pointwise comparison ($P < 0.01$); magenta line, global comparison ($P < 0.01$; for explanation, see MATERIALS AND METHODS; Fujisawa et al. 2008). *B*: same as in *A* from another pair with members recorded from the CA3 and CA1 regions. *C*: CCG matrix based on 26,406 simultaneously recorded neuron pairs ($n = 163$ neurons) in a single session. Red pixel: monosynaptic connection (based on significant short-latency peaks) with reference neuron as putative pyramidal cell ($n = 127$). White lines: separation of neurons recorded by *probe 1* and *probe 2*. Numbers identify the recording shanks. CCG shown in *A* and *B* are circled. *D*: circuit diagram reconstructed from monosynaptic connections (for shank orientation, see Fig. 2). Red triangles: excitatory neurons. Blue circles: putative inhibitory interneurons. Gray squares: unidentified neurons. Local and CA3-CA1 connections, marked with (a) and (b) (as shown in *A* and *B*), are highlighted by yellow. Note convergence of multiple pyramidal cells on target interneurons. The figure is a representative sample for illustration purposes only.

web site). Sharp wave-ripples are self-organized population patterns that arise in the CA3 region and depolarize the midapical dendrites of CA1 neurons as seen extracellularly by a large-amplitude negative wave in stratum radiatum (Ylinen et al. 1995). As expected, LFP activity before the occurrence of spikes during sharp wave-ripple events was most prominent in the CA1 s. radiatum (Fig. 12*A*; Supplemental Video S1). In contrast, during place-related activity, pyramidal cells are believed to be discharged by a combination of the direct entorhinal input terminating in s. lacunosum-moleculare and the CA3 input (Moser et al. 2008; Fig. 12*B*). During ambulation, LFP activity before spike occurrence was first observed in the s. lacunosum-moleculare and dentate molecular layer followed by the CA3 activation in CA1 s. radiatum before the spikes of the place cell. These findings illustrate the exceptional power of the combination of recording spikes and high spatial density monitoring of LFP for understanding the input-output transformation of single neurons.

Large-scale recordings from the mouse brain. Multiplexing neuronal signals is even more critical for recordings from mice because the size and weight of the preamplifiers and the connecting cable can seriously affect the behavioral performance of the animal. Either 32- or 64-channel headstages and their combinations are deployed for high-density recordings from 2 or 3 brain structures, including various neocortical areas, hippocampus, thalamus, nucleus accumbens, and ventral tegmental area. In addition to the multiplexed outputs, the recording headstage contains 2 detachable light-emitting diodes (LEDs) for tracking the animal's position with a video camera and a 3-dimensional accelerometer to monitor fast head movements. Figure 13*A* shows illustrative neocortical traces from a mouse exploring an open maze. The silicon probe

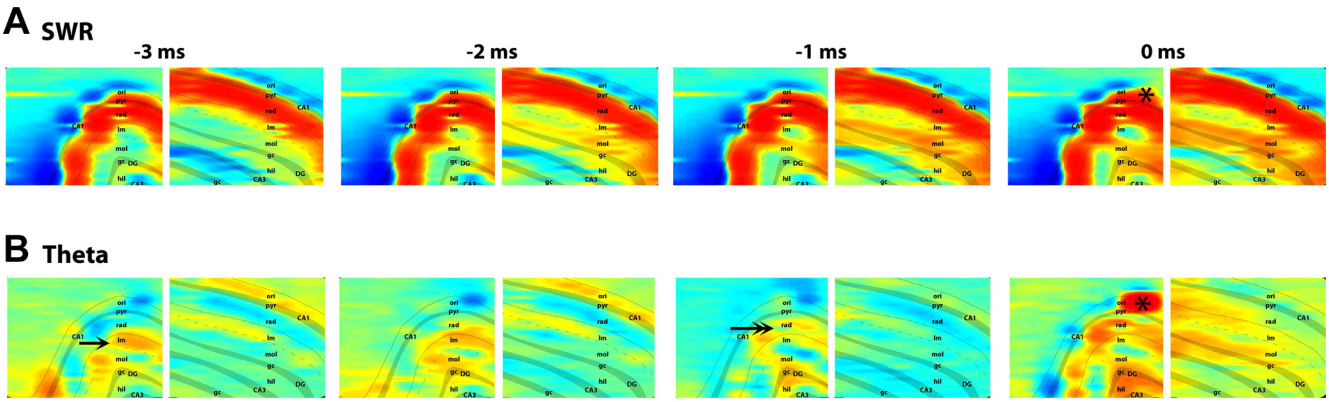

Fig. 12. Spikes are embedded in unique and spatially distributed LFP. Spike-triggered averages of the LFP in the hippocampus during slow-wave sleep (*A*) and exploration (*B*). During sleep, spikes were sampled during SWR; during exploration (theta), spikes of the same neuron were sampled while the rat ran on a linear track for a water reward. Recordings were made by 2 8-shank (300-μm intershank distance), 256-site silicon probes. The LFP was smoothed and interpolated both within and across shanks. The LFP was triggered by the spikes of a pyramidal neuron in CA1 pyramidal layer (pyr; shown by an asterisk). Both frame sequences show 4 50-μs-resolution snapshots of the LFP map before (-3 to -1 ms) and at the time of the spike occurrence (0 ms). The 2 images of each frame are showing the activities on the 2 probes (as shown in Fig. 9). Note that during sleep (*A*), activity arises (negative wave, hot colors) in CA3 and invades the CA1 stratum radiatum (rad). During exploration (*B*), the spike is associated with synaptic activity mainly in the s. lacunosum-moleculare (lm; shown by an arrow) followed by the radiatum layer (double arrow), indicating a combination of entorhinal cortex and CA3 input activation. The LFP map changes characteristically with time (see Supplemental Video S1). ori, Oriens layer; gc, granule cell layer; hil, hilus.

recordings are most often combined with optogenetic manipulation of the recorded neurons, using laser or LED-powered sharpened optical fibers that deliver light to the tips of the probe shanks (Berényi et al. 2012; Royer et al. 2010; Stark et al. 2012; Fig. 13*B*).

DISCUSSION

We have described a complete system that allows high-channel-count recordings from a small volume of neuronal tissue using a lightweight signal multiplexing headstage that permits free behavior such as exploration in mazes. This was achieved by multiple stages of development, including multi-shank high-density recording silicon probes, ultraflexible interconnect, miniaturized microdrive (Vandecasteele et al. 2012), and, most importantly, high-throughput on-stage signal multiplexing, remote-site digitization, and demultiplexing, which allow to link the animal to the recording/processing hardware by an ultralight cable. The system has been extensively tested for large-scale recordings of spike outputs and LFP signals in both rats and mice. The 2-D distribution of the recording sites distributed across several layers and regions can provide important information about the distribution of LFP together with large-scale unit recordings.

Sensing of electrical activity is complementary to optics-based imaging methods (Alivisatos et al. 2013). Silicon probes can access deep brain structures and offer sampling speed at the level of neuronal communication. They provide neuron-scale resolution in local circuits and permit the study of interactions of multiple brain regions, currently not practical with imaging methods (Ghosh et al. 2011). Electrodes are invasive, a feature that can be improved with further size reduction, refinement of tip configuration, and tissue-compatible coating (Du et al. 2011; Kipke et al. 2008; Wise et al. 2004). In the current configuration, the combined volume of the 8 recording shanks of the 256-site probe is comparable with the volume of 8 wire tetrodes (Wilson and McNaughton 1993) but can record from significantly larger numbers of units in addition to providing high-spatial-resolution LFP signals. Even the 8-shank, 64-site probe can record from >100 neurons (Fujisawa et al. 2008). In addition, linear probes have the advantage of online identification of the recording layers, the spatial localization of the main current sources and sinks, and the positions of the recorded neurons (Csicsvari et al. 2003). We present here a method to determine the position of the electrodes during experiments, exploiting the high within-layer gamma band coherence of the LFP. Polarity reversal of sleep spindles, K-complexes, and other LFP patterns can also be used to increase the precision of layer segregation. Since the layer identification we described is done in situ, it allows for the determination of the recordings sites in each session. This is a major advantage in experiments when the probe is moved gradually in the course of multiple sessions and for layer-restricted optical stimulation in future experiments.

The 50-μm spacing of the recording sites on the 256-site probe (Figs. 1*A* and 10) is suboptimal for unit recordings and cell clustering (Harris et al. 2000). Denser recording sites without increasing the shank volume is desirable. On the other hand, the additional 2-D recording of the LFP from multiple layers and regions is an additional benefit. Because of the rapid development of silicon technology, probes with >1,000 site counts and 20-μm site spacing, yet without further size increase, are expected in the near future. Ultimately, a dynamically reshapeable probe design (by selecting recording sites within the cellular layers with high-quality unit activity) would overcome the tradeoff of the current probe design by significantly improving the single-unit yield and still keeping the amount of recorded data reasonable.

In addition to significantly increasing the number of recording sites, the size of the multiplexers should also be considerably reduced. Although the size and weight of the extracranial devices is less of a problem in head-fixed animals, currently they are the most limiting factors in experiments that require free movement of small rodents. In the current configuration, silicon probes are connected to the multiplexers via an ultraflexible polyimide cable, but the multiplexers have to be manually soldered onto the printed circuit board. In addition to size

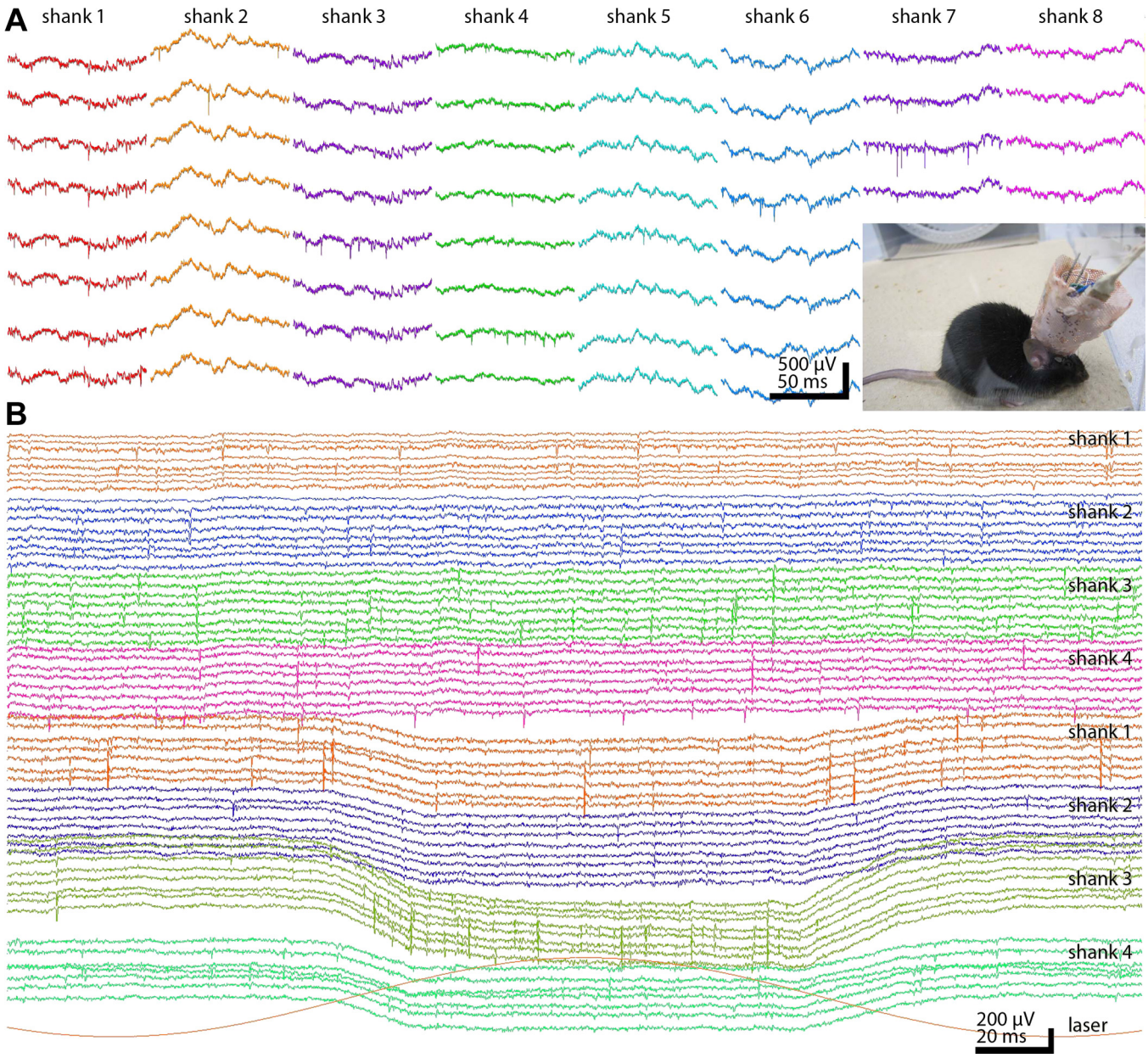

Fig. 13. Unit and LFP recordings from the mouse. *A*: chronic recordings from a mouse using an 8-shank 64-site silicon probe. One hundred-millisecond epochs from each shank are shown. *Inset*: headstage with silicon probe, microdrive, and 64-channel signal multiplexer surrounded by copper mesh shielding. The freely moving mouse is connected to the equipment by an ultraflexible cable. *B*: 2 4-shank, 32-site probes were placed in the nucleus accumbens (*top shanks 1-4*) and ventral tegmental area (VTA; *bottom shanks 1-4*) in a TH-Cre;Ai32 mouse, expressing ChR2 in tyrosine hydroxylase-expressing neurons. One of the shanks in the VTA also contained an optical fiber for light delivery (Stark et al. 2012). Note VTA neuronal responses to 472-nm (*bottom* red trace) laser light stimulation.

limitation, the numerous mechanical connections among the probe, interconnect, multiplexers, and the offsite demultiplexer increase failure rate.

In terms of the cluster quality of units, our system outperformed a benchmark commercial recording system. The relatively low input impedance of the Intan RHA-2132 multiplexer chip (13 MΩ at 1 kHz) and its relatively high-input capacitance (12 pF) attenuated the recorded signal by ~20%, comparing with another nonmultiplexed headstage. However, the serial, temporally noncoincident transmission of the multiple channel segments makes the multiplexer more resistant to mechanical cable artifacts. Signal attenuation of the multiplexer could be eliminated by adding buffer operational amplifiers before multiplexing. However, such modification may double the current size of the multiplexer, adding unwanted additional weight and volume to the headstage.

New generation probes may have on-probe signal amplification and multiplexing capabilities (Csicsvari et al. 2003; Olsson et al. 2005). Alternatively, the required signal multiplexing circuits can become an integral part of the flexible interconnect cable (Viventi et al. 2011). The use of flexible and active interface electronics may offer an alternative approach that may be advantageous for several applications. The digital output of the multiplexers (Harrison 2008) allows direct streaming of the neurophysiological data to the computer

without the extra step of A/D conversion. Digital multiplexers also offer noise reduction since potential noise sources of cable transmission, further amplification, and offsite digital conversion can be eliminated (Harrison 2008). In principle, amplification and multiplexing can be placed on the probe shanks, effectively reducing the required large numbers of interconnects between the recording sites and electronics outside of the brain. Unfortunately, current CMOS circuits require ~1-V supply voltage and may generate both excess heat and local electric fields that may modify the activity of nearby neurons if placed on the shank itself (Berényi et al. 2012). Thus, without dramatic reduction of the power consumption, brain-embedded electronics remain a major challenge (Alivisatos et al. 2013).

In principle, cables interconnecting the headstage and the recording system can be completely eliminated by telemetry. Although up to 64-channel telemetry systems have been successfully used in small animals (Greenwald et al. 2011; Harrison et al. 2011; Sodagar et al. 2007; Szuts et al. 2011) and may be the only solution for specific applications (Yartsev and Ulanovsky 2013), multiplexing and ultraflexible cables allow much higher bandwidth, higher channel counts, and lower noise. The power source required for telemetry adds weight and limits the duration of the experiments, especially in mice.

Computation in brain circuits is performed by numerous specialized neurons. Identification and manipulation of specific neuron types in the behaving animal has recently become possible with optogenetics (Boyden et al. 2005) combined with ever-increasing specificity of neuron labeling, mostly in mice (Madisen et al. 2012; Taniguchi et al. 2011). Therefore, perhaps the most important new direction should be the development of combined techniques that allow precise delivery of light locally to the simultaneously recorded neurons. Experiments have shown that as low as 5–15 μW of light is sufficient to activate ChR2-expressing neurons in vivo (Stark et al. 2012). However, construction and use of silicon probe devices with etched optical fibers that allow precise local delivery of light energy are currently done manually, and only few laboratories have the capability to use such methods routinely (Anikeeva et al. 2012; Royer et al. 2010, 2012; Stark et al. 2012). To bridge the gap between optogenetics and large-scale recording of neurons, there are at least two possible viable solutions. The first one is adding optical waveguides integrated into the shanks of the silicon probe and coupling the back end of the waveguides to lasers, LEDs, or laser diodes (Stark et al. 2012; Wu et al. 2013; Zorzos et al. 2010). The second option is integrating neuron-sized LED sources mixed with the recording sites on the silicon probe (Kim et al. 2013). Either configuration will offer unmatched spatial precision and capability of targeted perturbation and recording from specified neuron types. Integration of optical stimulation, large-scale recording, and on-stage multiplexing will facilitate the dissemination and use such tools in a large number of laboratories for the investigation of multiple circuits and their behavior-dependent interactions in freely moving small rodents for testing hypotheses of neural networks and brain function.

GRANTS

This study was supported by National Institutes of Health Grants NS-34994, MH-54671, and NS-074015, the Human Frontier Science Program, and the J. D. McDonnell Foundation. A. Berényi was supported by a Marie Curie FP7-PEOPLE-2009-IOF Grant (no. 254780), EU-FP7-ERC-2013-Starting Grant (no. 337075), the Momentum Program of the Hungarian Academy of Sciences, and the Rosztóczy Foundation.

DISCLOSURES

A. Berényi is the founder of Amplipex Ltd., Szeged, Hungary, which manufactures signal-multiplexed headstages and demultiplexing systems. The other authors declare the absence of any commercial or financial relationships that could be construed as a potential conflict of interest.

AUTHOR CONTRIBUTIONS

A.B., A.L., T.D.H., and G.B. conception and design of research; A.B., A.J.N., L.R., J.D.L., S.F., and E.S. performed experiments; A.B., Z.S., L.R., S.F., E.S., and G.B. analyzed data; A.B., Z.S., L.R., J.D.L., S.F., E.S., and G.B. interpreted results of experiments; A.B., Z.S., and G.B. prepared figures; A.B. and G.B. drafted manuscript; A.B., Z.S., A.J.N., L.R., J.D.L., S.F., E.S., A.L., T.D.H., and G.B. edited and revised manuscript; A.B., Z.S., A.J.N., L.R., J.D.L., S.F., E.S., A.L., T.D.H., and G.B. approved final version of manuscript.

REFERENCES

Alivisatos AP, Chun M, Church GM, Deisseroth K, Donoghue JP, Greenspan RJ, McEuen PL, Roukes ML, Sejnowski TJ, Weiss PS, Yuste R. Neuroscience. The brain activity map. *Science* 339: 1284–1285, 2013.

Alivisatos AP, Chun M, Church GM, Greenspan RJ, Roukes ML, Yuste R. The brain activity map project and the challenge of functional connectomics. *Neuron* 74: 970–974, 2012.

Anikeeva P, Andalman AS, Witten I, Warden M, Goshen I, Grosenick L, Gunaydin LA, Frank LM, Deisseroth K. Optetrode: a multichannel readout for optogenetic control in freely moving mice. *Nat Neurosci* 15: 163–170, 2012.

Barthó P, Hirase H, Monconduit L, Zugaro M, Harris KD, Buzsáki G. Characterization of neocortical principal cells and interneurons by network interactions and extracellular features. *J Neurophysiol* 92: 600–608, 2004.

Berényi A, Belluscio M, Mao D, Buzsáki G. Closed-loop control of epilepsy by transcranial electrical stimulation. *Science* 337: 735–737, 2012.

Blanche TJ, Spacek MA, Hetke JF, Swindale NV. Polytrodes: high-density silicon electrode arrays for large-scale multiunit recording. *J Neurophysiol* 93: 2987–3000, 2005.

Boyden ES, Zhang F, Bamberg E, Nagel G, Deisseroth K. Millisecond-timescale, genetically targeted optical control of neural activity. *Nat Neurosci* 8: 1263–1268, 2005.

Buzsáki G. Large-scale recording of neuronal ensembles. *Nat Neurosci* 7: 446–451, 2004.

Buzsáki G, Anastassiou CA, Koch C. The origin of extracellular fields and currents–EEG, ECoG, LFP and spikes. *Nat Rev Neurosci* 13: 407–420, 2012.

Carandini M. From circuits to behavior: a bridge too far? *Nat Neurosci* 15: 507–509, 2012.

Csicsvari J, Henze DA, Jamieson B, Harris KD, Sirota A, Barthó P, Wise KD, Buzsáki G. Massively parallel recording of unit and local field potentials with silicon-based electrodes. *J Neurophysiol* 90: 1314–1323, 2003.

Du J, Blanche TJ, Harrison RR, Lester HA, Masmanidis SC. Multiplexed, high density electrophysiology with nanofabricated neural probes. *PLoS One* 6: e26204, 2011.

Du J, Riedel-Kruse IH, Nawroth JC, Roukes ML, Laurent G, Masmanidis SC. High-resolution three-dimensional extracellular recording of neuronal activity with microfabricated electrode arrays. *J Neurophysiol* 101: 1671–1678, 2009.

Fujisawa S, Amarasingham A, Harrison MT, Buzsáki G. Behavior-dependent short-term assembly dynamics in the medial prefrontal cortex. *Nat Neurosci* 11: 823–833, 2008.

Ghosh KK, Burns LD, Cocker ED, Nimmerjahn A, Ziv Y, Gamal AE, Schnitzer MJ. Miniaturized integration of a fluorescence microscope. *Nat Methods* 8: 871–878, 2011.

Greenwald E, Mollazadeh M, Hu C, Wei T, Culurciello E, Thakor V. A VLSI neural monitoring system with ultra-wideband telemetry for awake behaving subjects. *IEEE Trans Biomed Circuits Syst* 5: 112–119, 2011.

Harris KD, Henze DA, Csicsvari J, Hirase H, Buzsáki G. Accuracy of tetrode spike separation as determined by simultaneous intracellular and extracellular measurements. *J Neurophysiol* 84: 401–414, 2000.

Harrison RR. The design of integrated circuits to observe brain activity. *Proc IEEE* 96: 1203–1216, 2008.

Harrison RR, Fotowat H, Chan R, Kier RJ, Olberg R, Leonardo A, Gabbiani F. Wireless neural/EMG telemetry systems for small freely moving animals. *IEEE Trans Biomed Circuits Syst* 5: 103–111, 2011.

Henze DA, Borhegyi Z, Csicsvari J, Mamiya A, Harris KD, Buzsáki G. Intracellular features predicted by extracellular recordings in the hippocampus in vivo. *J Neurophysiol* 84: 390–400, 2000.

Hirabayashi T, Takeuchi D, Tamura K, Miyashita Y. Microcircuits for hierarchical elaboration of object coding across primate temporal areas. *Science* 341: 191–195, 2013.

Kim TI, McCall JG, Jung YH, Huang X, Siuda ER, Li Y, Song J, Song YM, Pao HA, Kim RH, Lu C, Lee SD, Song IS, Shin G, Al-Hasani R, Kim S, Tan MP, Huang Y, Omenetto FG, Rogers JA, Bruchas MR. Injectable, cellular-scale optoelectronics with applications for wireless optogenetics. *Science* 340: 211–216, 2013.

Kipke DR, Shain W, Buzsáki G, Fetz E, Henderson JM, Hetke JF, Schalk G. Advanced neurotechnologies for chronic neural interfaces: new horizons and clinical opportunities. *J Neurosci* 28: 11830–11838, 2008.

Lein ES, Hawrylycz MJ, Ao N, Ayres M, Bensinger A, Bernard A, Boe AF, Boguski MS, Brockway KS, Byrnes EJ, Chen L, Chen L, Chen TM, Chin MC, Chong J, Crook BE, Czaplinska A, Dang CN, Datta S, Dee NR, Desaki AL, Desta T, Diep E, Dolbeare TA, Donelan MJ, Dong HW, Dougherty JG, Duncan BJ, Ebbert AJ, Eichele G, Estin LK, Faber C, Facer BA, Fields R, Fischer SR, Fliss TP, Frensley C, Gates SN, Glattfelder KJ, Halverson KR, Hart MR, Hohmann JG, Howell MP, Jeung DP, Johnson RA, Karr PT, Kawal R, Kidney JM, Knapik RH, Kuan CL, Lake JH, Laramee AR, Larsen KD, Lau C, Lemon TA, Liang AJ, Liu Y, Luong LT, Michaels J, Morgan JJ, Morgan RJ, Mortrud MT, Mosqueda NF, Ng LL, Ng R, Orta GJ, Overly CC, Pak TH, Parry SE, Pathak SD, Pearson OC, Puchalski RB, Riley ZL, Rockett HR, Rowland SA, Royall JJ, Ruiz MJ, Sarno NR, Schaffnit K, Shapovalova NV, Sivisay T, Slaughterbeck CR, Smith SC, Smith KA, Smith BI, Sodt AJ, Stewart NN, Stumpf KR, Sunkin SM, Sutram M, Tam A, Teemer CD, Thaller C, Thompson CL, Varnam LR, Visel A, Whitlock RM, Wohnoutka PE, Wolkey CK, Wong VY, Wood M, Yaylaoglu MB, Young RC, Youngstrom BL, Yuan XF, Zhang B, Zwingman TA, Jones AR. Genome-wide atlas of gene expression in the adult mouse brain. *Nature* 445: 168–176, 2007.

Lichtman JW, Denk W. The big and the small: challenges of imaging the brain's circuits. *Science* 334: 618–623, 2011.

Logothetis NK. The underpinnings of the BOLD functional magnetic resonance imaging signal. *J Neurosci* 23: 3963–3971, 2003.

Madisen L, Mao T, Koch H, Zhuo JM, Berenyi A, Fujisawa S, Hsu YW, Garcia AJ 3rd, Gu X, Zanella S, Kidney J, Gu H, Mao Y, Hooks BM, Boyden ES, Buzsáki G, Ramirez JM, Jones AR, Svoboda K, Han X, Turner EE, Zeng H. A toolbox of Cre-dependent optogenetic transgenic mice for light-induced activation and silencing. *Nat Neurosci* 15: 793–802, 2012.

Mizuseki K, Sirota A, Pastalkova E, Buzsáki G. Theta oscillations provide temporal windows for local circuit computation in the entorhinal-hippocampal loop. *Neuron* 64: 267–280, 2009.

Montgomery SM, Sirota A, Buzsáki G. Theta and gamma coordination of hippocampal networks during waking and rapid eye movement sleep. *J Neurosci* 28: 6731–6741, 2008.

Moser EI, Kropff E, Moser MB. Place cells, grid cells, and the brain's spatial representation system. *Annu Rev Neurosci* 31: 69–89, 2008.

Nicolelis MA, Ghazanfar AA, Faggin BM, Votaw S, Oliveira LM. Reconstructing the engram: simultaneous, multisite, many single neuron recordings. *Neuron* 18: 529–537, 1997.

O'Keefe J, Nadel L. *The Hippocampus as a Cognitive Map*. Oxford, UK: Clarendon Press, 1978.

Olsson RH 3rd, Buhl DL, Sirota AM, Buzsaki G, Wise KD. Band-tunable and multiplexed integrated circuits for simultaneous recording and stimulation with microelectrode arrays. *IEEE Trans Biomed Eng* 52: 1303–1311, 2005.

Prakash R, Yizhar O, Grewe B, Ramakrishnan C, Wang N, Goshen I, Packer AM, Peterka DS, Yuste R, Schnitzer MJ, Deisseroth K. Two-photon optogenetic toolbox for fast inhibition, excitation and bistable modulation. *Nat Methods* 9: 1171–1179, 2012.

Ray S, Maunsell JH. Different origins of gamma rhythm and high-gamma activity in macaque visual cortex. *PLoS Biol* 9: e1000610, 2011.

Royer S, Zemelman BV, Barbic M, Losonczy A, Buzsáki G, Magee JC. Multi-array silicon probes with integrated optical fibers: light-assisted perturbation and recording of local neural circuits in the behaving animal. *Eur J Neurosci* 31: 2279–2291, 2010.

Royer S, Zemelman BV, Losonczy A, Kim J, Chance F, Magee JC, Buzsáki G. Control of timing, rate and bursts of hippocampal place cells by dendritic and somatic inhibition. *Nat Neurosci* 15: 769–775, 2012.

Sirota A, Montgomery S, Fujisawa S, Isomura Y, Zugaro M, Buzsáki G. Entrainment of neocortical neurons and gamma oscillations by the hippocampal theta rhythm. *Neuron* 60: 683–697, 2008.

Sodagar AM, Wise KD, Najafi K. A fully integrated mixed-signal neural processor for implantable multichannel cortical recording. *IEEE Trans Biomed Eng* 54: 1075–1088, 2007.

Stark E, Koos T, Buzsáki G. Diode probes for spatiotemporal optical control of multiple neurons in freely moving animals. *J Neurophysiol* 108: 349–363, 2012.

Szuts TA, Fadeyev V, Kachiguine S, Sher A, Grivich MV, Agrochao M, Hottowy P, Dabrowski W, Lubenov EV, Siapas AG, Uchida N, Litke AM, Meister M. A wireless multi-channel neural amplifier for freely moving animals. *Nat Neurosci* 14: 263–269, 2011.

Taniguchi H, He M, Wu P, Kim S, Paik R, Sugino K, Kvitsiani D, Fu Y, Lu J, Lin Y, Miyoshi G, Shima Y, Fishell G, Nelson SB, Huang ZJ. A resource of Cre driver lines for genetic targeting of GABAergic neurons in cerebral cortex. *Neuron* 71: 995–1013, 2011.

Tye KM, Deisseroth K. Optogenetic investigation of neural circuits underlying brain disease in animal models. *Nat Rev Neurosci* 13: 251–266, 2012.

Vandecasteele M, M S, Royer S, Belluscio M, Berényi A, Diba K, Fujisawa S, Grosmark A, Mao D, Mizuseki K, Patel J, Stark E, Sullivan D, Watson B, Buzsáki G. Large-scale recording of neurons by movable silicon probes in behaving rodents. *J Vis Exp* 61: e3568, 2012.

Viventi J, Kim DH, Vigeland L, Frechette ES, Blanco JA, Kim YS, Avrin AE, Tiruvadi VR, Hwang SW, Vanleer AC, Wulsin DF, Davis K, Gelber CE, Palmer L, Van der Spiegel J, Wu J, Xiao J, Huang Y, Contreras D, Rogers JA, Litt B. Flexible, foldable, actively multiplexed, high-density electrode array for mapping brain activity in vivo. *Nat Neurosci* 14: 1599–1605, 2011.

Wilson MA, McNaughton BL. Dynamics of the hippocampal ensemble code for space. *Science* 261: 1055–1058, 1993.

Wise KD, Anderson DJ, Hetke JF, Kipke DR, Najafi K. Wireless implantable microsystems: high-density electronic interfaces to the nervous system. *Proc IEEE* 92: 76–97, 2004.

Wu F, Stark E, Im M, Cho IJ, Yoon ES, Buzsáki G, Wise KD, Yoon E. An implantable neural probe with monolithically integrated dielectric waveguide and recording electrodes for optogenetics applications. *J Neural Eng* 10: 056012, 2013.

Yartsev MM, Ulanovsky N. Representation of three-dimensional space in the hippocampus of flying bats. *Science* 340: 367–372, 2013.

Yizhar O, Fenno LE, Davidson TJ, Mogri M, Deisseroth K. Optogenetics in neural systems. *Neuron* 71: 9–34, 2011.

Ylinen A, Bragin A, Nádasdy Z, Jandó G, Szabó I, Sik A, Buzsáki G. Sharp wave-associated high-frequency oscillation (200 Hz) in the intact hippocampus: network and intracellular mechanisms. *J Neurosci* 15: 30–46, 1995.

Zorzos AN, Boyden ES, Fonstad CG. Multiwaveguide implantable probe for light delivery to sets of distributed brain targets. *Opt Lett* 35: 4133–4135, 2010.